The Astrophysical Journal, 914:16 (23pp), 2021 June 10 https://doi.org/10.3847/1538-4357/abf63c

NGC 5128 Globular Cluster Candidates Out to 150 kpc: A Comprehensive Catalog from Gaia and Ground-based Data*

Allison K. Hughes[1], David J. Sand[1], Anil Seth[2], Jay Strader[3], Karina Voggel[4], Antoine Dumont[2], Denija Crnojević[5], Nelson Caldwell[6], Duncan A. Forbes[7], Joshua D. Simon[8], Puragra Guhathakurta[9], and Elisa Toloba[10]

[1] Steward Observatory, University of Arizona, 933 North Cherry Avenue, Tucson, AZ 85721, USA; akhughes@email.arizona.edu
[2] Department of Physics & Astronomy, University of Utah, Salt Lake City, UT 84112, USA
[3] Center for Data Intensive and Time Domain Astronomy, Department of Physics and Astronomy, Michigan State University, East Lansing, MI 48824, USA
[4] Universite de Strasbourg, CNRS, Observatoire astronomique de Strasbourg, UMR 7550, F-67000 Strasbourg, France
[5] University of Tampa, 401 West Kennedy Boulevard, Tampa, FL 33606, USA
[6] Center for Astrophysics, Harvard & Smithsonian, 60 Garden Street, Cambridge, MA 02138, USA
[7] Centre for Astrophysics and Supercomputing, Swinburne University of Technology, Hawthorn VIC 3122, Australia
[8] Observatories of the Carnegie Institution for Science, 813 Santa Barbara Street, Pasadena, CA 91101, USA
[9] UCO/Lick Observatory, University of California Santa Cruz, 1156 High Street, Santa Cruz, CA 95064, USA
[10] Department of Physics, University of the Pacific, 3601 Pacific Avenue, Stockton, CA 95211, USA
Received 2021 February 12; revised 2021 March 26; accepted 2021 April 3; published 2021 June 9

Abstract

We present a new catalog of 40,502 globular cluster (GC) candidates in NGC 5128 out to a projected radius of ∼150 kpc based on data from the Panoramic Imaging Survey of Centaurus and Sculptor, the Gaia Data Release 2, and the NOAO Source Catalog. Ranking these candidates based on the likelihood that they are true GCs, we find that approximately 1900 belong to our top two ranking categories and should be the highest priority for spectroscopic follow-up for confirmation. Taking into account our new data and a vetting of previous GC catalogs, we estimate a total GC population of 1450 ± 160 GCs. We show that a substantial number of sources previously argued to be low-velocity GCs are instead foreground stars, reducing the inferred GC velocity dispersion. This work showcases the power of Gaia to identify slightly extended sources at the ∼4 Mpc distance of NGC 5128, enabling accurate identification of GCs throughout the entire extended halo, not just the inner regions that have been the focus of most previous work.

Unified Astronomy Thesaurus concepts: Globular star clusters (656); Optical identification (1167); Galaxy evolution (594)

Supporting material: FITS files, machine-readable table

1. Introduction

Globular clusters (GCs) are an essential tool for understanding the formation, structure, and evolution of galaxies beyond the Local Group, where spectroscopy of individual stars is typically difficult or impossible (see the reviews of Harris 1991; Brodie & Strader 2006; Beasley 2020). These old, massive ($\gtrsim 10^4\ M_\odot$) star clusters are found in all but the least luminous galaxies. The majority of GCs are associated with the stellar halo, where they serve as luminous beacons of the underlying low surface brightness stellar population. With modern wide-field imagers and spectrographs, GCs can be used to measure the mass and structure of dark matter halos (e.g., Alabi et al. 2016; Wasserman et al. 2018) and trace individual accretion events (e.g., Mackey et al. 2010).

Historically, NGC 5128 (Centaurus A) has been a leading target for extragalactic GC studies due to its richness and proximity. It is the central elliptical galaxy in a small group of galaxies at a distance of 3.8 ± 0.1 Mpc (Harris et al. 2010). Since the first discovery of GCs in NGC 5128 in the 1980s, many photometric and spectroscopic surveys have been conducted, leading to the identification of 557 confirmed GCs and thousands of GC candidates (Graham & Phillips 1980; van den Bergh et al. 1981; Hesser et al. 1986; Harris et al. 1992, 2004, 2012; Harris et al. 2002, 2006; Holland et al. 1999; Martini & Ho 2004; Peng et al. 2004; Woodley et al. 2005, 2007, 2010a, 2010b; Gómez et al. 2006; Rejkuba et al. 2007; Beasley et al. 2008; Georgiev et al. 2009, 2010; Mouhcine et al. 2010; Sinnott et al. 2010; Taylor et al. 2010, 2015, 2017; Fahrion et al. 2020; Müller et al. 2021; Voggel et al. 2020). The majority of these studies have focused on the inner ∼40 kpc of the galaxy. Both the presence of halo substructures out to ≳100 kpc (Crnojević et al. 2016, 2019) and the fact that the total GC population of NGC 5128 is likely in the range of ∼1000–2000 clusters (e.g., Harris et al. 2006; Harris 2010; Taylor et al. 2017) illustrate that there is substantial room for novel studies of the NGC 5128 GC system, especially in the outer halo.

While the proximity of NGC 5128 aids in the identification and follow-up of GC candidates, this close distance also provides several challenges. First, the halo of NGC 5128 is spread across $\gtrsim 20\ \mathrm{deg}^2$ of sky (Crnojević et al. 2016), requiring large area searches for a comprehensive accounting of the stellar halo and GC system. The galaxy is also relatively close to the Galactic plane (with a Galactic latitude of $b \sim 19°$), leading to significant contamination from foreground stars, as well as foreground extinction ($E(B-V) \sim 0.12$ mag; Schlafly & Finkbeiner 2011). An additional issue is that with a modest systematic velocity of $541\ \mathrm{km\ s^{-1}}$ (Hui et al. 1995) and a velocity dispersion of $\sigma \sim 150\ \mathrm{km\ s^{-1}}$ (Wilkinson et al. 1986;

* This paper includes data gathered with the 6.5 m Magellan Telescope at Las Campanas Observatory, Chile.

Silge et al. 2005), there is some overlap in the radial velocity of NGC 5128 GCs and Milky Way foreground stars; radial velocity alone cannot definitively give membership for every object, especially on the low-velocity end of the distribution (see Appendix B).

The Panoramic Imaging Survey of Centaurus and Sculptor (PISCeS) produced a wide-field resolved stellar map of NGC 5128 out to a projected galactocentric radius of ∼150 kpc (Crnojević et al. 2016). The PISCeS data are invaluable in searching for GCs because of the survey's wide angular coverage and good seeing (median FWHM of 0.″66), which allows GCs at the distance of NGC 5128 to be marginally resolved and hence separated from foreground stars.

Here we take advantage of this exquisite data set to build a new wide-field catalog of GC candidates, focusing especially on the outer halo (projected radii ∼40–150 kpc) that is nearly unexplored with spectroscopy. We supplement our high-quality PISCeS imaging with other data from the second Gaia data release (DR2) and the NOAO Source Catalog (NSC) to refine our sample, with a future goal of comprehensive spectroscopic follow-up.

The PISCeS data are well suited to identify typical GCs outside the central regions of NGC 5128. In a companion paper (Voggel et al. 2020, hereafter V20), our team focused on the related question of constructing a complete sample of the most luminous GCs and stripped galaxy nuclei in NGC 5128. This requires a distinct approach, as many of these sources are saturated or crowded in the PISCeS data.

This paper is organized as follows. Section 2 outlines the key data sets used in our GC candidate search. In Section 3, we identify a fiducial sample of known radial velocity–confirmed NGC 5128 GCs that we use to define our GC candidate selection methodology, which we describe in Section 4. Our final catalogs are presented in Section 5, and further results are discussed in Section 6. We summarize and conclude in Section 7. In Appendix A, we present a collected catalog of all confirmed NGC 5128 GCs as a resource for the community. In Appendix B, we provide information detailing foreground stars, identified by their Gaia parallax or proper-motion measurements, that were previously misreported as NGC 5128 GCs and report and resolve other discrepancies in the NGC 5128 GC literature when possible. Throughout this work, we adopt a distance modulus for NGC 5128 of $(m-M)_0 = 27.91$ mag, corresponding to a distance of $D = 3.82$ Mpc (Harris et al. 2010). The physical scale at this distance is 18.5 pc arcsec^{-1} (1.1 kpc arcmin^{-1}).

2. Key Data Sets

2.1. The PISCeS Survey

The foundational data set of our GC search is deep NGC 5128 Magellan/Megacam imaging from the PISCeS survey. Here we briefly describe the relevant aspects of the survey strategy and observational methods; for further details, see Crnojević et al. (2014, 2016, 2019).

The goal of the PISCeS survey is to image the halos of the nearby massive galaxies NGC 5128 and NGC 253 (NGC 253 is not covered in this paper; see Sand et al. 2014 and Toloba et al. 2016) out to a projected radius of $R \sim 150$ kpc. The data are deep enough to reach ∼1–2 mag below the tip of the red giant branch (RGB) ($r \sim 25.5$–26.5 mag). These uniquely deep wide-field maps enable discovery of faint dwarf galaxies and other halo substructures, such as tidal streams and shells, allowing comparisons with similar observations in the Local Group (e.g., McConnachie et al. 2009).

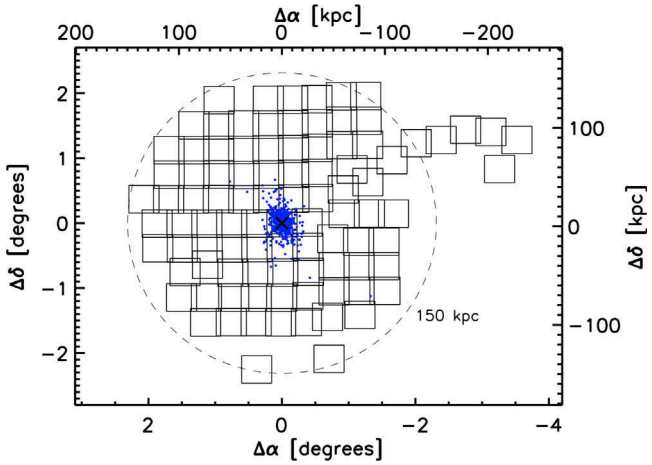

Figure 1. Footprint of the PISCeS survey around NGC 5128, using data from 2010 to 2017, comprising 95 separate Magellan/Megacam fields, and oriented such that north is up and east is left. The dashed circle marks a radius of 150 kpc from the center of NGC 5128, located at $\alpha = 201.^\circ362540$, $\delta = -43.^\circ033627$, which is marked by the central black cross. The blue dots mark the positions of known confirmed GCs around NGC 5128, which are largely confined to the central ∼40 kpc. Note that several pointings in this map were not presented in the dwarf galaxy luminosity function analysis of Crnojević et al. (2019) but are included here: an extension to the northwest, two pointings to the south centered on known dwarfs KK 203 and KK 196, and data that were not high enough quality for a dwarf search but were sufficiently deep for our GC search.

The PISCeS survey uses the Megacam imager (McLeod et al. 2015) on the 6.5 m Magellan Clay telescope. With the $f/5$ secondary, Megacam has an $\sim 24' \times 24'$ field of view with a binned (2×2) scale of 0.″16 pixel^{-1}. We tiled the halo of NGC 5128 with individual pointings of this size, as illustrated in Figure 1. The typical exposure times were 6×300 s in both the g and r bands but were adjusted depending on the seeing and sky conditions to try to achieve a similar depth in poorer seeing or nonphotometric conditions.

The data were reduced in the standard manner at the Smithsonian Astrophysical Observatory Telescope Data Center, including bias subtraction, flat-fielding, and cosmic-ray rejection. As part of this reduction, an ICRS astrometric solution based on the Two Micron All Sky Survey point-source catalog (Cutri et al. 2003) was applied, and the images of a given field and filter were stacked with `SWARP` (Bertin 2010). Subsequent to this processing, the release of Gaia DR2 allowed us to check this astrometry. Cross-matching found a mean PISCeS–Gaia DR2 offset of ($\alpha \cos\delta$, δ) of (0.″1300 ± 0.″0002, 0.″0634 ± 0.″0002). These values are consistent across the fields and subsamples of PISCeS. We do not correct the self-consistent astrometry of PISCeS to the Gaia DR2 frame.

Photometric calibration was done by observing Sloan Digital Sky Survey (Ahumada et al. 2020) equatorial fields on photometric nights at a variety of airmasses. We designed intentional ∼2′ overlaps between NGC 5128 fields to allow for cross-calibration of the entire survey, leveraging data taken on photometric nights. All photometry is on the AB mag system. This paper includes data from 95 pointings around NGC 5128 obtained between 2010 and 2017, as illustrated in Figure 1. The footprint includes nearly full coverage of the area out to

∼150 kpc from the center of the galaxy and an arm extending in the northwest direction out to ∼260 kpc.

For GC candidate photometry, we ran `SExtractor` (Bertin & Arnouts 1996) on the g and r stacked images. Aperture photometry was done using aperture diameters of 3 and 6 pixels (0.″48 and 0.″96, respectively), with the intention of using the differences between these magnitudes to select extended sources, including GCs. We also measure the "total" magnitudes for each source in our catalog at a diameter of $6 \times$ FWHM (for the median seeing, this is a radius of ∼12.4 pixels = 2.″0), with an aperture correction determined on a field-by-field basis. When relevant, we correct the photometry for foreground Galactic extinction using the maps of Schlafly & Finkbeiner (2011) on a source-by-source basis. We are explicit about when a correction for extinction is (or is not) made throughout this work, and all absolute magnitudes are extinction-corrected. Finally, we combine the g and r catalogs using a matching radius of 1″. Our use of PISCeS data to select GC candidates is detailed in Sections 4.1–4.4.

GCs are luminous; the peak of the lognormal GC luminosity function (GCLF) is expected to occur at $M_r \sim -7.7$ (Pota et al. 2015) with $\sigma \sim 1.3$ mag (Jordán et al. 2007), corresponding to an observed peak near $r \sim 20.5$. This means that the PISCeS survey, designed for depths of $r \sim 26$–26.5, is quite effective at photometry of typical GCs around NGC 5128. However, we have issues with recovering the most luminous GCs and ultracompact dwarfs (UCDs), which are up to ∼10 mag (a factor of 10,000) brighter than our targeted individual red giants. PISCeS data start to saturate for point sources with $r \lesssim 18$ ($M_r \lesssim -10.2$) in the median field, with this limit pushed to $r \lesssim 18.6$–18.8 ($M_r \lesssim -9.6$ to -9.4) for the few pointings with the best seeing or highest background. For this reason, in our companion paper, V20, we take an approach that relies only partially on the PISCeS data to make a complete catalog of the most luminous sources.

2.2. Gaia DR2

Gaia is an ongoing all-sky astrometric space mission. Its DR2 presents at least some astrometric and photometric measurements for over a billion sources down to a broadband $G \sim 21$ mag (Gaia Collaboration et al. 2018b).

Gaia DR2 is a useful adjunct to the PISCeS data in two areas. First, through its measurements of proper motion and parallax, it allows us to identify and remove a large fraction of Galactic foreground stars that would otherwise contaminate our GC candidate sample. Second, with an effective angular resolution of ∼0.″4 (Evans et al. 2018), Gaia DR2 includes astrometric and photometric statistics that can be used to pinpoint even marginally extended sources, such as GCs in NGC 5128.

We explain our use of Gaia DR2 to identify NGC 5128 GCs in Section 4.4. The newly available Gaia Early Data Release 3 (Gaia Collaboration et al. 2021) and other future updates will provide additional and higher-quality data for sources, increasing the accuracy with which we can identify nearby extragalactic GCs.

2.3. NOAO Source Catalog

The NSC is a unified collection of nearly all of the public data taken on the Dark Energy Camera (DECam) on the Blanco 4 m telescope at CTIO, as well as the Mosaic3 imager on the 4 m Mayall telescope at KPNO (Nidever et al. 2018). It includes our area of interest around NGC 5128, with typical depths of $u \sim 23.3$, $g \sim 21.7$, $r \sim 21.2$, $i \sim 21.2$, and $z \sim 21.0$. For this work, we have used Data Release 1 of the NSC, although Data Release 2 has recently become available (Nidever et al. 2021).

GCs have spectral energy distributions that are distinct from both individual foreground stars and background galaxies with extended star formation histories. However, the single color available from PISCeS ($g - r$) does an inadequate job at separating these populations. The multicolor photometry available in the NSC provides yet another method to identify and remove Milky Way foreground stars that would otherwise contaminate our GC candidate sample. We explain the use of the NSC to identify NGC 5128 GCs via their color in Section 4.5.

To bring together data obtained under different protocols and by multiple PIs, Nidever et al. (2018) reprocessed the raw data with consistent quality control, selection, and calibration. Astrometric calibration with Gaia DR1 was done for each chip independently. Photometric calibration was done with model magnitudes constructed for their filters from public all-sky catalogs and the Schlegel et al. (1998) reddening map for the extinction term. There is a fairly consistent, color-dependent offset between the PISCeS and NSC photometry between ±0.1 mag in the r band and 0.05 and 0.17 mag in the g band. We provide information about both PISCeS and NSC photometry in our final catalog of GC candidates.

The NSC includes the same data that comprise the Survey of Centaurus A's Baryonic Structures (SCABS), a wide-field *ugriz* imaging survey of NGC 5128 using DECam (Taylor et al. 2016, 2017, hereafter T17). A list of likely NGC 5128 GC candidates out to ∼140 kpc based on color and some structural information is provided by T17. We do not use the SCABS data catalogs directly because (i) the PISCeS data generally have higher image quality (median FWHM = 0.″66) than the SCABS data (FWHM ∼ 0.″8–1.″2); (ii) it is clear from intercomparisons of PISCeS, NSC, and SCABS that the latter suffers from field edge effects and significant, inconsistent magnitude offsets; and (iii) the NSC has a higher completeness for known GCs than SCABS. We also note in passing that Table 2 of T17 appears to be extinction-corrected, despite the statements in the table caption and text that it has not been (we hope this information helps future researchers using these data). Within the PISCeS footprint, the NSC contains the reprocessed raw data from SCABS and other surveys with consistent quality control, selection, and calibration that results in a catalog with higher quality than SCABS alone.

3. A Fiducial Sample of Radial Velocity–Confirmed GCs

To help guide and assess the fidelity of our GC candidate selection, we first build a fiducial sample of radial velocity–confirmed GCs in NGC 5128. We find an initial set of 630 "confirmed" GCs by cross-matching published samples (Graham & Phillips 1980; van den Bergh et al. 1981; Harris et al. 1992; Harris et al. 2002, 2006; Peng et al. 2004; Woodley et al. 2005, 2007, 2010a, 2010b; Rejkuba et al. 2007; Beasley et al. 2008; Georgiev et al. 2009, 2010; Taylor et al. 2010; Fahrion et al. 2020; Müller et al. 2021; V20). The most common way to confirm a GC is based on its radial velocity, though some studies instead rely on morphological parameters or visual classification with Hubble Space Telescope (HST) imaging.

Updated Gaia DR2 and radial velocity measurements for many of these sources show that 73 objects are not actually GCs in NGC 5128; see Appendix B for details. Removing this contamination leaves a cleaned list of 557 confirmed GCs around NGC 5128, which we discuss and provide in Table 4 in Appendix A.

For the specific goals of this paper, we select a subset of these confirmed GCs to guide our selection process. Each GC in this fiducial sample (i) is $>10'$ from the center of NGC 5128, (ii) has a radial velocity $>250\,\mathrm{km\,s^{-1}}$, (iii) is in the Gaia DR2 catalog and does not have proper-motion and parallax values consistent with being in the foreground, (iv) has not been marked as a foreground star or background galaxy in any catalog, and (v) has photometry in our PISCeS `SExtractor` catalogs and the NSC. This leaves a set of 69 fiducial GCs, as noted in Table 4, that can be used to test all of the criteria we use for selecting GCs outside the central regions of NGC 5128. We think that nearly all of the GCs in the larger, cleaned sample of 557 confirmed objects are true GCs associated with NGC 5128, and we use this broader list to assess the completeness of our sample in Section 6.3.

In addition to our fiducial sample of GCs, we also construct similar sets of foreground stars and background galaxies that have been confirmed via radial velocity measurements or HST imaging, as found by previous studies of NGC 5128 (Peng et al. 2004; Woodley et al. 2005; Gómez et al. 2006; Harris et al. 2006; Beasley et al. 2008). These confirmed contaminant samples allow independent tests of the precision of our GC selection techniques.

4. Identifying GC Candidates

This section describes the process of finding GC candidates within the 95 calibrated images from the PISCeS survey, incorporating data from Gaia DR2 and NSC. A summary is given in Section 4.6.

To assess the effectiveness of each step of our selection process, we compare our results with our fiducial sample of confirmed GCs and catalogs of known foreground stars and background galaxies. Information from each part of our selection process is used to calculate a final GC likelihood score between zero and 1 for each candidate, where a score of 1 corresponds to those most likely to be true GCs in NGC 5128. Where possible, we prioritize completeness over purity in each step of our selection process, though we recognize the limitations that our data sets have in regard to the brightest and faintest GCs.

4.1. Initial Cuts

At the bright end, we remove saturated or nearly saturated sources, which typically have $r \lesssim 18$ mag (see also Section 4.2). We use a faint magnitude limit of 22 mag in the band (g or r) with better seeing. A magnitude of $g = 22$ mag is $\sim$0.7 mag (a factor of $\sim$1.9 in luminosity) beyond the turnover of the GCLF. Fainter than this limit, contamination grows substantially, and ancillary information from Gaia DR2 and NSC is either absent or of lower quality. We use the same limit with the r band ($r < 22$ mag) to help remove spurious sources, since essentially all true GCs have $g - r > 0$. Finally, we restrict our study to projected distances greater than $10'$ from the center of NGC 5128, as crowding strongly affects our photometry in this inner region. Much of this central area is already covered by high-quality HST data and other GC surveys.

We do not include in our candidate catalog any objects that have been confirmed in previous NGC 5128 studies as background galaxies or foreground stars via radial velocity measurements or HST imaging, unless specifically noted in Table 6 in Appendix B.2.

4.2. Concentration Index

Milky Way GCs range in half-light radius from 1 to 20 pc (with a mean of $\approx$3 pc), corresponding to $0\farcs05$–$1\farcs08$ at the distance of NGC 5128. In the excellent seeing of the PISCeS data (median FWHM of $0\farcs66$), this means that GCs are slightly extended compared to point sources. The most massive and largest GCs can be readily identified by the resolved stars along their outskirts (see also V20).

We can utilize the extended nature of GCs in NGC 5128 to separate them from foreground stars in the Milky Way using a concentration index–magnitude diagram. This method has been commonly used in previous extragalactic GC studies to separate candidate GCs from foreground stars or background galaxies, both from the ground and with HST (Whitmore et al. 1999; Peng et al. 2011; Durrell et al. 2014; Beasley & Trujillo 2016; Peng & Lim 2016; Ko et al. 2019).

To calculate the concentration indices, for each field, we measure the difference in magnitudes at diameters of 3 and 6 pixels ($0\farcs48$ and $0\farcs96$, respectively) for each source. These aperture sizes were chosen to be effective at separating true GCs from contaminants under a range of crowding and signal-to-noise ratio conditions. Because the image quality differs among the 95 fields, the mean magnitude difference for foreground stars varies between 0.72 and 1.28 mag, with a standard deviation in the range 0.01–0.07 mag. To create a concentration index that can be compared among fields, we select unsaturated point sources with magnitudes between 18.5 and 20.0 and normalize the distribution of magnitude differences to a mean of zero and a standard deviation of 1 on a per-field basis after trimming the outliers.[11] Figure 2 shows the concentration index–magnitude diagram for all sources between $10'$ and $30'$ of NGC 5128, highlighting the separation of the fiducial sample GCs from foreground stars. We use the symbol C_{3-6} to represent these normalized values, where larger C_{3-6} values correspond to more extended sources.

Assuming that point sources are distributed in a Gaussian distribution centered around $C_{3-6} = 0$, the *concentration_likelihood* for each GC candidate is defined as 1 minus the probability that the candidate's C_{3-6} value is consistent with a point source. For this calculation, we use data from the observing band (g or r) with better seeing. As an example, if a candidate has $C_{3-6} = 2.0$, it lies 2σ above the point-source average for that field, and we assign it a *concentration_likelihood* of 0.977.

Stars that are nearly saturated lead to C_{3-6} values above zero at bright magnitudes, even for true point sources (see stars with $r \lesssim 18$ in Figure 2). We exclude these saturated (or nearly saturated) objects. Reliably identifying the most luminous GCs and ultracompact dwarfs requires a separate set of selection criteria, discussed in V20.

[11] Using the IDL code `resistant_mean`. All robust means and standard deviations calculated in this paper use the same code.

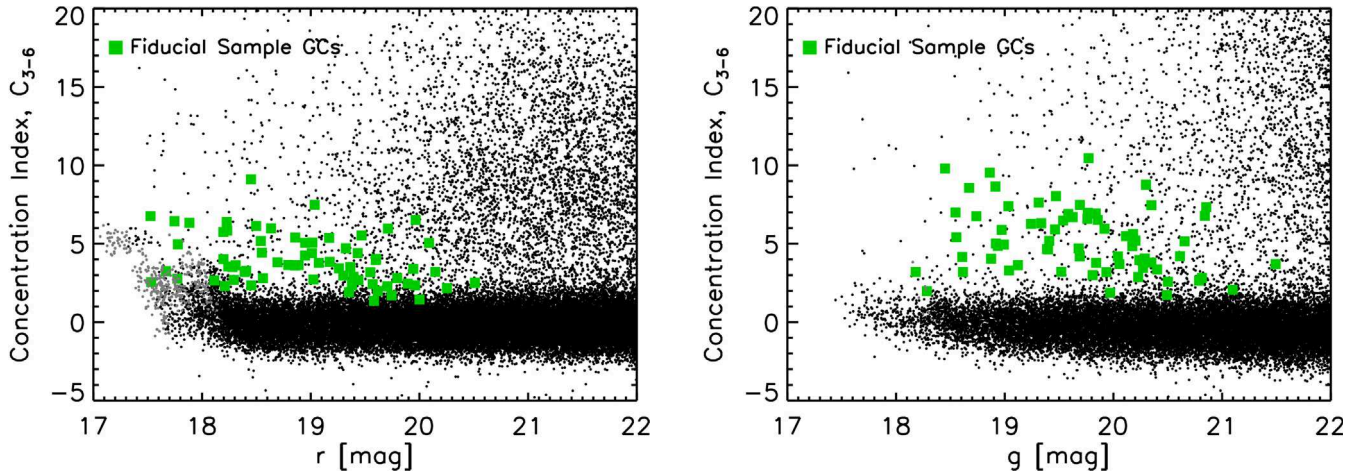

Figure 2. Concentration index (C_{3-6}) for fiducial sample GCs (green squares) and all sources between 10′ and 30′ of the center of NGC 5128 (black dots). The left panel shows *r*-band data, and the right panel shows *g*-band data. Objects with a larger C_{3-6}, such as GCs and background galaxies, are extended compared to point-source foreground stars. Objects plotted in gray have been removed due to saturation/near saturation at brighter magnitudes.

All of the fiducial sample GCs have C_{3-6} values greater than 1.3 in the *r* band and 1.7 in the *g* band, corresponding to *concentration_likelihood* values greater than 0.912 and 0.958, respectively. The average C_{3-6} value of the fiducial GCs is 3.9 in the *r* band and 5.2 in the *g* band. For each candidate, we use the band with better seeing to calculate its likelihood, noting that the fiducial sample is recovered with high purity in both bands.

We compiled all available size information for GCs in NGC 5128 (Rejkuba et al. 2007; McLaughlin et al. 2008; Taylor et al. 2010, 2015). Only 16 of the 69 fiducial sample GCs have physical size information, with half-light radii between ≈2.1 and 4.9 pc and an average of 3.0 pc. The smallest of these has a concentration index of 1.7 in the *r* band and 4.1 in the *g* band. Because most searches are not sensitive to the most compact GCs and our selection cuts are based on previously known GCs, our final catalog may also not include the smallest GCs (half-light radius ≈1–2 pc) in NGC 5128.

All sources in the 95 PISCeS fields that passed the initial cuts and have a *concentration_likelihood* > 0.84 ($C_{3-6} > 1.0$) are passed as GC candidates to the next stage of the selection process.

4.3. Removing Galaxies and Blends

Besides GCs, there are other types of extended sources in the PISCeS data. Among objects with higher values of concentration index ($C_{3-6} > 3$), there is a substantial contribution from background galaxies, especially toward fainter magnitudes. Due to the relatively low Galactic latitude of NGC 5128 ($b = 19°$), blends or near-blends of foreground stars are also common. Figure 3 shows visual examples of both true GCs and common contaminants.

The process described in this section aims to reduce contamination from background galaxies and stellar blends in our final GC candidate catalog by analyzing the shape and brightness profile of each of our potential GC candidate targets.

We build an algorithm that produces a binary output, identifying a source as being either (1) too elliptical and/or extended to be a GC in NGC 5128, in which case it is given a structure-based likelihood (*structure_check*) of zero, or (2) round and only slightly extended, as expected for GCs, in which case it is given *structure_check* = 1. This algorithm was designed empirically such that a majority of visually identifiable galaxies receive *structure_check* = 0, while the fiducial sample GCs receive *structure_check* = 1.

The galaxy/blend assessment that produces this final binary output is a three-step process. For each source, we first take the `SExtractor` `flux_radius` parameter, which measures the circular-equivalent effective radius (the circular aperture radius enclosing half the total flux of an object) in units of pixels. We then compare this to a conservative limit, which is a robust average `flux_radius` of foreground stars in the field +3 pixels, tuned to pass even marginal GC candidates and exclude the more obvious galaxies. Objects above this critical value are given *structure_check* = 0, while those with `flux_radius` values below the limit continue to the next step.

We next check the ellipticity of the candidates, motivated by the fact that true GCs are mostly round, while background galaxies (and blends) have a broader ellipticity distribution. The ellipticity ϵ is defined as $\epsilon = 1 - b/a$, where *a* and *b* are the semimajor and semiminor axes measured by `SExtractor`. We reject the source (set *structure_check* = 0) if $\epsilon > 0.35$ in one of the *g* and *r* bands and $\epsilon > 0.25$ in the other. A few of the most massive star clusters around NGC 5128 have ellipticities up to $\epsilon \sim 0.35$, likely related to their origin as stripped galaxy nuclei (Voggel et al. 2018). Hence, our ellipticity cut could, in principle, remove a small number of sources truly associated with NGC 5128. Since the current paper is focused on typical GCs rather than the most massive objects, this ellipticity cut represents an important step in removing the contaminants that are abundant at fainter magnitudes.

As a final evaluation of how extended the brightness profiles of individual candidates are, in each band, we measure the magnitude of each target in concentric apertures of diameter 12, 20, 28, and 36 pixels and determine the magnitude differences between successive pairs (diff_12_20, diff_20_28, and diff_28_36). For this step, we reject the source (set *structure_check* = 0) as too extended if all three of the following conditions are met in either the *g* or *r* band: (i) diff_12_20 is 10 times greater than the aperture correction value (see Section 2.1), (ii) diff_20_28 > 0.1, and (iii) diff_28_36 > 0.1. These larger apertures effectively remove extended, moderately round background galaxies that passed

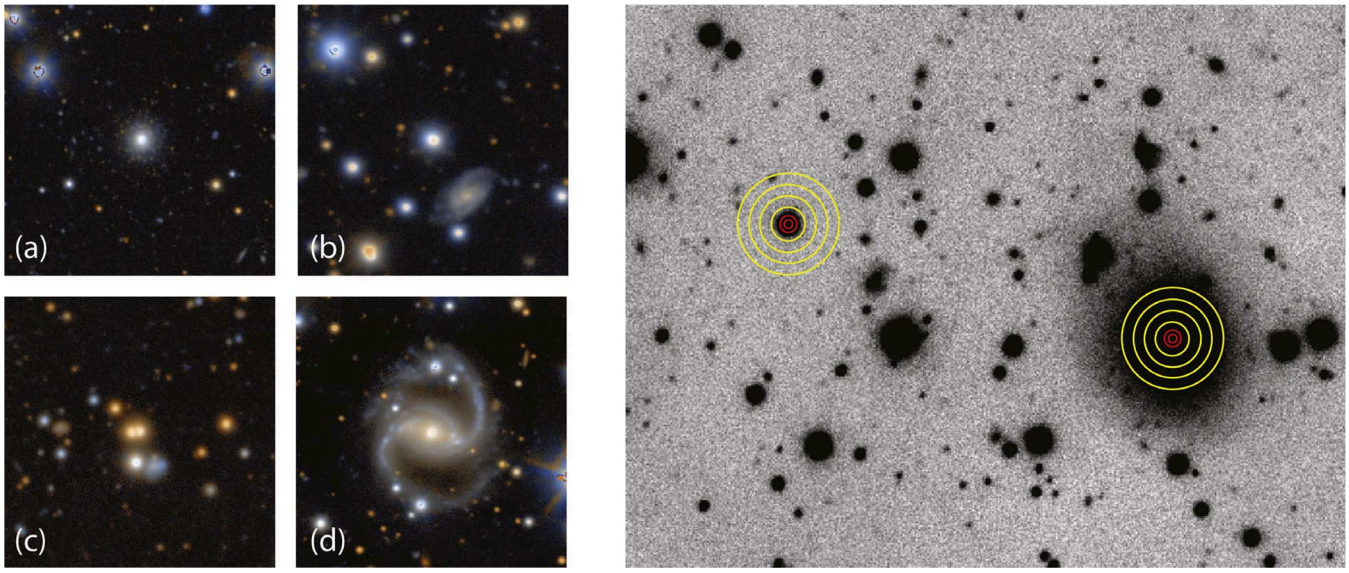

Figure 3. Examples of extended objects with $C_{3-6} > 3$. In the left panel, we show (a) a confirmed, luminous GC (KV 19-442) that is partially resolved, with red giants apparent in its outskirts; (b) a good GC candidate that is not resolved into stars but is extended compared to a point source; (c) a pair of foreground stars that are close enough that they are photometered as a single source with a large C_{3-6} value; and (d) a very extended galaxy that is cut during the galaxy removal process (Section 4.3). Each image is $\approx 1' \times 1'$. In the right panel, we show an example of how a GC can be distinguished from a background galaxy by using a brightness profile compiled from a series of concentric apertures with 12, 20, 28, and 36 pixel diameters (yellow circles). The smaller red circles show the 3 and 6 pixel diameter apertures used for the concentration index measurements.

the previous selection steps. See Figure 3 for a visual example of this process.

As a test of this galaxy/blend removal step, we compare our results with the velocity-confirmed background galaxies from several previous spectroscopic studies of GCs around NGC 5128 (Peng et al. 2004; Woodley et al. 2005; Gómez et al. 2006; Beasley et al. 2008). These sources were originally selected in a variety of ways but generally had colors and magnitudes consistent with those expected for GCs. We find that the steps in this subsection identify 58 out of 95 (61%) unique background galaxies from these previous studies. It is reasonable to assume that a subset of the more obvious background galaxies were culled prior to spectroscopy in these studies. Therefore, our selection steps can be expected to successfully flag and remove a large fraction of background galaxies in our magnitude range.

By examining the confirmed background galaxies not identified by our selection steps, we find that these are marginally extended and circular and hence visually similar to true GCs. As we discuss below, additional photometric or spectroscopic information is needed to reliably reject these remaining background galaxies.

In total, 66% of the possible GC candidates that meet the criteria detailed at the end of Section 4.2 are given *structure_check* = 1, and the other 34% are given *structure_check* = 0 and removed from the GC candidate sample.

4.4. Gaia DR2

Section 2.2 briefly introduced the possibility of using Gaia DR2 to improve our GC catalog both in relatively straightforward ways (by removing foreground stars) and in a more unexpected fashion (by identifying marginally resolved sources). Here we discuss how we use a range of astrometric and photometric Gaia DR2 measurements in our GC candidate selection process.

First, we note that 305 of the 557 confirmed NGC 5128 GCs (55%) are in Gaia DR2. About 80% of the missing objects are faint ($g > 20$ in PISCeS or NSC) and likely below the DR2 completeness limit (Boubert & Everall 2020). Most of the rest are within 10′ of the galaxy center (where photometry is difficult) or have conflicting literature classifications (see Appendix B.2 for details).

Of the GC candidates that passed the galaxy/blend removal step in Section 4.3, we find that 62% of these sources are in Gaia DR2. If a source is not in DR2, it is simply passed to the color selection in Section 4.5. Likewise, if a source is in Gaia DR2 but has a missing measurement (such as the BP/RP excess factor discussed below), we simply skip the evaluation of the relevant step.

4.4.1. Proper Motion and Parallax

The proper motions and parallaxes of objects associated with NGC 5128 cannot be measured with Gaia DR2. Therefore, any sources with significant proper motions or parallaxes can be identified as being in the foreground and removed from the GC candidate sample.

We first calculate the total proper motion of an object by adding the R.A. and decl. components in quadrature. Assuming the combined proper motion has a χ distribution with two degrees of freedom, it can be simplified to a Rayleigh distribution. We assign a *proper_motion_likelihood* of 1–CDF, where CDF is the cumulative distribution function of the Rayleigh distribution. Sources with lower *proper_motion_likelihood* values are therefore more likely to be foreground stars based on their proper-motion measurements. For example, if the proper motion is significant at 2σ, the likelihood assigned is $1 - 0.865 = 0.135$. We truncate this at 3σ (0.011); sources with proper motions more significant than this value are given *proper_motion_likelihood* = 0 and removed from the candidate list.

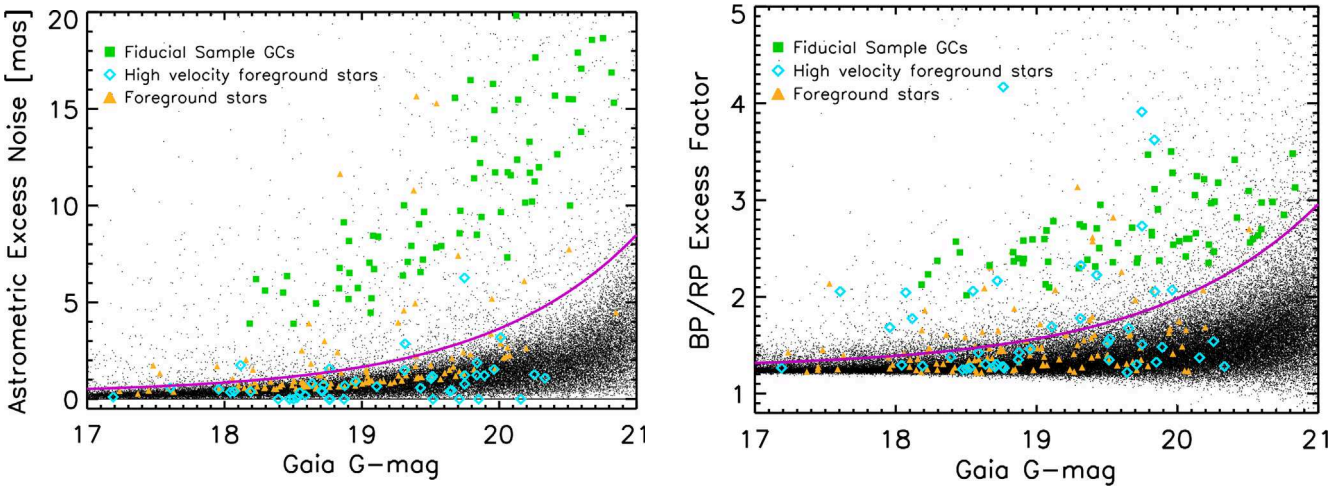

Figure 4. Left: plot of Gaia's AEN parameter vs. G-band magnitude. Right: plot of Gaia's BR_{excess} parameter vs. G-band magnitude. In both plots, the black dots are all Gaia DR2 sources between 10′ and 60′ of NGC 5128, the green squares are fiducial sample GCs, the blue diamonds are foreground stars based on their proper motion (discussed in Appendix B.1), and the orange triangles are radial velocity–confirmed foreground stars. The fiducial sample GCs are distinct from the general population of foreground stars in both parameter spaces, so we can use the AEN and BR_{excess} parameters to identify GC candidates. The lines denoting 3σ are given by Equations (1) and (2). Confirmed foreground stars with AEN or BR_{excess} values greater than 3σ are stellar blends, visible in PISCeS images.

We also calculate a similar *parallax_likelihood* based on the significance of the parallax, here assuming the measurement has a Gaussian distribution. For example, if the parallax is significant at 2σ, the likelihood assigned is $1 - 0.954 = 0.046$. Sources with $>3\sigma$ parallax measurements are given *parallax_likelihood* $= 0$ and removed from the candidate list. Since significant parallax measurements are much less common than significant proper-motion measurements in Gaia DR2, it is rare to have an object with a significant parallax but not a significant proper motion.

Of the GC candidates in Gaia DR2 that passed the galaxy/blend removal step in Section 4.3, we find that 68% are removed for having proper-motion and/or parallax measurements consistent with being foreground stars.

Of the 391 confirmed foreground stars in previously published papers, 313 (80%) are identified using these *proper_motion_likelihood* and *parallax_likelihood* criteria. The remainder have insignificant proper motions or parallaxes or are not in Gaia DR2, primarily because they are faint. This comparison shows that Gaia is an effective tool to identify and remove foreground stars from our GC candidate sample.

4.4.2. Astrometric Excess Noise

Gaia DR2 reports the astrometric excess noise (AEN) as a statistic that quantifies the goodness of fit of their five-parameter astrometric model to the astrometry for each target (Gaia Collaboration et al. 2018a). The AEN, given in units of milliarcseconds, is equal to zero for a well-fit star and has larger values for poorer fits. Objects that are extended compared to point sources have large AEN values, and in V20, we showed that this can be used to select marginally resolved objects such as GCs around NGC 5128.

In Figure 4, we plot AEN versus Gaia DR2 G mag for sources around NGC 5128. Most of these are foreground stars and therefore have low AEN values ($\lesssim 1$), especially at brighter magnitudes where the random uncertainties are smaller. This figure also plots the fiducial sample GCs, showing that they have larger AEN values and are largely distinct from foreground stars. Much like the concentration index C_{3-6}, AEN is more valuable for rejecting foreground stars than for rejecting extended objects such as background galaxies or foreground star blends, which, like GCs, will have higher AEN values.

Because the AEN distribution depends on the Gaia DR2 G mag, we determined a robust AEN mean and standard deviation for point sources in 0.1 mag bins. We then calculate a candidate's *aen_likelihood* as 1 minus the probability that its AEN value is consistent with a point source at that magnitude, truncating the distribution at -2σ (*aen_likelihood* $= 0.023$). Rather than an error, each AEN value is also reported with a corresponding "significance" measure, where a value greater than 2 indicates that the given AEN is probably significant. Because a majority of sources with high AEN values are not single stars, they have bad astrometric fits and therefore high significance values.

As an example calculation, consider a GC candidate with an AEN value of 2.14 mas and Gaia DR2 $G = 20.03$ mag. In the bin between $G = 20.0$ and 20.1 mag, foreground stars have an AEN robust mean of 1.465 mas and $\sigma = 0.672$ mas. This GC candidate is 1σ above the mean for point sources and therefore has an *aen_likelihood* of 0.841.

For the convenience of the reader who wishes to have a simple criterion to find extended sources in other circumstances, we use information from Gaia DR2 for sources in the radial range 10′–60′ from the galaxy center to define a line 3σ above the mean foreground star AEN value,

$$\mathrm{AEN}_{3\sigma} = 0.297 + 5.63 \times 10^{-8}\, e^{0.895\, G}, \qquad (1)$$

where G is the Gaia DR2 G mag. This line is plotted in Figure 4. We emphasize that for this paper, we use the likelihood analysis described above.

All of the 69 fiducial sample GCs are greater than 4σ above the mean AEN for foreground stars at their magnitude. Of the 375 confirmed foreground stars in Gaia DR2, 345 (92%) have AEN values within 3σ of the mean for their G magnitude. Visual inspection using PISCeS imaging shows that the remaining 30 stars with large AEN values are all close blends. This confirms the utility of AEN for rejecting single foreground stars from the GC candidate catalog.

4.4.3. BP/RP Excess Factor

As we previously showed in V20, a second Gaia DR2 parameter useful for finding extended sources is the BP/RP excess factor (BR_{excess}). This parameter gives the ratio of the sum of the flux of the blue photometer (BP; 3300–6800 Å) plus the red photometer (RP; 6400–10500 Å) with the flux in the broadband G filter. Its utility comes from the distinct manner in which these fluxes are determined; the BP and RP magnitudes are measured directly from the flux within a large aperture of 3.4×2.1 arcsec^2, while the G magnitude is derived from profile fitting with an effective resolution of $\sim 0\farcs4$ (Evans et al. 2018). This difference means that extended sources have a higher BR_{excess} than point sources, since fitting an effective point-source profile to an extended source in G misses some of the light. As for the concentration index C_{3-6} and AEN, we expect all extended objects, including contaminant background galaxies and foreground star blends, to have large BR_{excess} values, while Galactic foreground stars will have small values.

Figure 4 (right panel) shows BR_{excess} plotted against Gaia DR2 G mag. Qualitatively the figure is similar to the corresponding one for AEN, with elevated BR_{excess} values for the fiducial sample of GCs and a clear point-source track of foreground stars. The fiducial GCs are less clearly separated from the stars than for AEN, but the data used are essentially independent, so it serves as a second valuable piece of information to find extended sources. We calculate a *bre_likelihood* for each candidate in the same manner as for *aen_likelihood*, described in Section 4.4.2.

We also constructed a similar line 3σ above the mean foreground star BR_{excess} value,

$$BR_{excess,3\sigma} = 1.26 + 2.79 \times 10^{-8}\, e^{0.853\, G}, \quad (2)$$

where G is the Gaia DR2 G mag.

All of the fiducial sample GCs have a BR_{excess} value at least 3σ above the mean BR_{excess} for foreground stars at their magnitude, and 90% of them have a BR_{excess} value above 4σ, excluding a single fiducial GC that does not have a BR_{excess} measurement.

Of the 367 confirmed foreground stars with BR_{excess} data, 300 (80%) have BR_{excess} values within 3σ of the mean for their magnitude. Reflecting what is seen with AEN, the remainder are mostly foreground star blends.

While both AEN and BR_{excess} measure how extended sources are in Gaia DR2—and hence are correlated for truly extended sources—the statistics are largely independent and hence valuable.

4.5. Color Selection

As old stellar populations with typically simple star formation histories, GCs have a restricted range of spectral energy distributions, governed primarily by metallicity. A fortunate side effect is that GCs occupy a limited area of parameter space in optical color–color diagrams, allowing them to be separated from foreground stars and background galaxies with reasonable fidelity. Hence, color–color diagrams have a long history in the selection of extragalactic GCs (e.g., Rhode & Zepf 2001; Strader et al. 2011; Brodie et al. 2014; Jennings et al. 2014; Powalka et al. 2016b; T17). The use of a wide spectral baseline, such as including the UV, near-IR, or both, improves the purity of the GC selection (Muñoz et al. 2014; Powalka et al. 2016a).

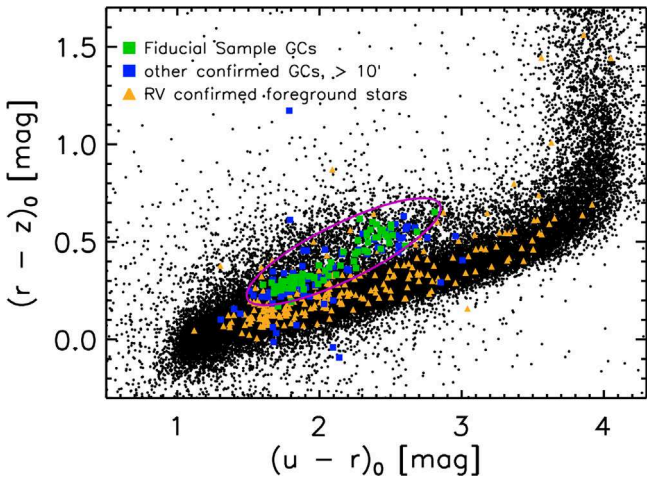

Figure 5. Optical color–color diagram of all sources at distances between 10′ and 60′ of NGC 5128 that are in both PISCeS and NSC. Almost all of the fiducial sample GCs (green squares) lie in a well-defined region that is separate from the radial velocity–confirmed foreground stars (orange triangles). The purple ellipse marks the elliptical region used to select GC candidates, which was chosen to bound the fiducial sample GCs and confirmed GCs at a distance greater than 10′ from the center of the galaxy.

Since our PISCeS data have only two filters (g and r bands), to use the color selection method, we match our catalog with NSC, which has *ugriz* photometry for over 100,000 sources within the PISCeS footprint (Nidever et al. 2018). Following the methods of past GC selection techniques, we use the u, r, and z filters to maximize the separation of GCs from foreground stars.

Figure 5 shows the position in $(u-r)_0$–$(r-z)_0$ space of all sources in the radial range 10′–60′ from the center of NGC 5128 that are in both PISCeS and NSC. The subscript zero (e.g., u_0) denotes that the photometry has been corrected for foreground Galactic extinction. For the purposes of calculating a likelihood, we define the high-probability GC area as an ellipse centered at $(u-r)_0 = 2.17$ and $(r-z)_0 = 0.45$, with semimajor axis 0.72 mag, semiminor axis 0.15 mag, and a position angle 19° from the x-axis, as illustrated in Figure 5. This ellipse encloses most of the fiducial GCs and the confirmed GCs outside of 10′ from the center of the galaxy. Using integrated single stellar population magnitudes from Marigo et al. (2008), we find that the cutoff in color on the blue side of the ellipse corresponds to GC models with ages $\gtrsim$5 Gyr at an [Fe/H] = −2 and $\gtrsim$1–2 Gyr for more metal-rich stellar populations.

To calculate the color-based likelihood, we draw 10,000 random samples from the u, r, and z bands for each source, assuming Gaussian photometric uncertainties. The fraction of these samples that lie within the ellipse is the *color_likelihood*. If all samples are within the ellipse, *color_likelihood* = 1. Since a few fiducial objects sit just outside the ellipse, and a few true GCs could have abnormal colors (e.g., due to a problem with their photometry in a single band), we set the minimum likelihood at 2σ (0.023), as we did for some of the Gaia DR2–based likelihoods. Candidates not in the NSC do not have their total likelihood values affected by this step.

As an example calculation, let us look at a typical GC candidate with $u_0 = 21.42 \pm 0.12$, $r_0 = 18.81 \pm 0.01$, and $z_0 = 18.28 \pm 0.03$. This candidate's position in color–color space of $(u-r)_0 = 2.61$ and $(r-z)_0 = 0.53$ is inside of the color selection ellipse, but only 80% of the randomly varied

samples drawn are within the ellipse. Therefore, it has *color_likelihood* = 0.80.

Out of the 69 fiducial sample GCs, 64 (93%) have *color_likelihood* > 0.95. Of all of the potential GC candidates that pass the concentration index, galaxy, and proper-motion/parallax tests, 29% have NSC photometry, and of these, 16% have *color_likelihood* > 0.75 and 4% have *color_likelihood* = 1.0. This suggests that the NSC color information is very effective in reducing the remaining contaminants in the GC candidate catalog.

4.6. Summary of GC Candidate Selection Process

To summarize, there are five steps in our GC candidate selection process for the 95 PISCeS fields. We first exclude the brightest and faintest candidates and those affected by crowding near the galaxy's center. We then do a likelihood-based selection of extended objects using a two-aperture technique on the PISCeS photometry. In the next step, background galaxies and stellar blends are rejected using cuts in the effective radius, ellipticity, and flux distribution at large radii. The penultimate step uses Gaia DR2 for a likelihood-based assessment that a source is a GC rather than a foreground star based on measurements of its astrometric motion (proper motion and parallax) and whether it is extended (AEN and BP/RP excess). Finally, we use multiband photometry from the NSC to assign a likelihood that each source has colors consistent with confirmed GCs.

The above likelihoods are multiplied together to give the *total_likelihood* of each candidate. Numbers closer to 1 represent a larger chance that the source is a GC, while candidates that did not survive a yes/no cut (i.e., those assigned a likelihood of zero at any point) have a *total_likelihood* = 0. These latter objects do not appear in our final GC catalog.

The different steps do not have their likelihoods normalized, and no penalties are applied if a target does not appear in a given catalog. For instance, if a GC candidate is not in the Gaia DR2 catalog because it is too faint, it is implicitly given a likelihood of 1 at that step. The interpretation of sources with different supporting data is considered in the next section, where these likelihoods are discussed in the context of our full PISCeS catalog.

5. Catalogs

In this section, we present two catalogs. The first includes all of our GC candidates, and the second includes all PISCeS sources that pass the initial cuts (see Section 4.1). We discuss these catalogs and how we rank our candidates based on the amount of data available for each.

5.1. GC Candidate and Overall Source Catalogs

The first presented catalog includes the 40,502 GC candidates in NGC 5128 found through our GC candidate selection process, as detailed in Section 4. We consider a PISCeS source to be a viable GC candidate if it has $C_{3-6} > 1.0$ and survives applicable yes/no cuts (initial cuts, *structure_likelihood*, *proper_motion_likelihood*, *parallax_likelihood*; see Sections 4.1, 4.3 and 4.4). The likelihood values for each candidate are multiplied together, and a reported *total_likelihood* value closer to 1.0 represents a GC candidate with a larger chance of being a true GC in NGC 5128.

Table 1 lists the header information for the catalog of GC candidates, which includes (1) a unique "H21" ID, which we assign; (2) discovery ID; (3) and (4) PISCeS R.A. and decl. in J2000 coordinates; (5)–(8) PISCeS g and r magnitudes and errors; (9) concentration index (C_{3-6}); (10) Gaia DR2 G magnitude; (11)–(18) proper motion in the R.A. and decl. directions, parallax, AEN, and BR_{excess} from Gaia DR2; and (19) and (20) NSC $(u-r)_0$ and $(r-z)_0$ color with Milky Way dust correction applied on a source-by-source basis (Schlafly & Finkbeiner 2011). We also list a breakdown of the likelihood values (21)–(27) *concentration_likelihood*, *proper_motion_likelihood*, *parallax_likelihood*, *aen_likelihood*, *bre_likelihood*, *color_likelihood*, and *total_likelihood* and (28) gold, silver, bronze, and copper rank (see below). For completeness, we (29) include and note targets that have previously been confirmed as GCs and (30) list all literature references. All PISCeS and Gaia DR2 photometry reported here has not been corrected for Galactic extinction. We do not include any GC candidates from the literature that are outside the PISCeS footprint or within 10′ of the center of NGC 5128. The full GC candidate table will be available online in electronic format.

The second catalog includes all PISCeS sources that pass our initial cuts (Section 4.1). In addition to GC candidates, this source catalog includes background galaxies and foreground stars that were removed by various steps in our GC candidate selection process. Along with the columns listed in the GC candidate table, we include information about the concentration index from both the PISCeS g and r bands, *structure_check*, Gaia DR2 R.A. and decl. in ICRS coordinates, and uncorrected NSC u, g, r, i, z photometry and errors. The header information is listed in Table 2. The full PISCeS source table will be available online in electronic format.

5.2. GC Candidate Data Rank

As a guide for future researchers who may use this GC candidate catalog for spectroscopic follow-up, we split our candidates into four categories ("gold," "silver," "bronze," and "copper") based on the number of our key data sets they appear in (see Table 3), separate from their quality (i.e., *total_likelihood*).

Gold GC candidates have data from PISCeS, Gaia DR2, and NSC. This group of GC candidates is expected to have the lowest amount of contamination from foreground stars and background galaxies at high *total_likelihood* scores, because they have information from all three key data sets pointing to the same result. The trade-off is that the gold group does not include faint GCs, as illustrated by the right panel of Figure 10. This is primarily due to the lack of Gaia DR2 sources at $G \gtrsim 20$ mag, which is ∼0.5 mag brighter than the NGC 5128 peak of the GCLF (Pota et al. 2015). Of the confirmed GCs outside of 10′ (see Appendix A), 42% have information in all three data sets. There are 5763 GC candidates in the gold category, of which 181 have *total_likelihood* ⩾ 0.85, which we identify as a good threshold in Section 6.1 because it maximizes the number of GC candidates above the background. The gold sample displays a clear overdensity of candidates near NGC 5128, which we discuss further below. Of the gold sample candidates between 10′ and 30′ (32.4 kpc), 15 have *total_likelihood* ⩾ 0.85 and have not been observed spectroscopically. This suggests that more GCs will be confirmed by following up this sample both close to and far from the center of the galaxy.

Table 1
Header Information for the Catalog of GC Candidates in NGC 5128

Column	Label	Description
1	ID	Unique "H21" ID
2	Discovery_ID	Discovery ID, if available
3	RA	PISCeS R.A. in decimal degrees (J2000)
4	Dec	PISCeS decl. in decimal degrees (J2000)
5	PISCeS_gmag	PISCeS g-band magnitude (mag)
6	PISCeS_gmag_err	Error of PISCeS g-band magnitude (mag)
7	PISCeS_rmag	PISCeS r-band magnitude (mag)
8	PISCeS_rmag_err	Error of PISCeS r-band magnitude (mag)
9	C_3_6	Concentration index value
10	Gaia_Gmag	Gaia DR2 G-band magnitude (mag)
11	pm_ra	Gaia DR2 proper-motion measurement in R.A. direction (mas yr^{-1})
12	pm_ra_err	Error of Gaia DR2 proper-motion measurement in R.A. direction (mas yr^{-1})
13	pm_dec	Gaia DR2 proper-motion measurement in decl. direction (mas yr^{-1})
14	pm_dec_err	Error of Gaia DR2 proper-motion measurement in decl. direction (mas yr^{-1})
15	parallax	Gaia DR2 parallax measurement (mas)
16	parallax_err	Error in Gaia DR2 parallax measurement (mas)
17	AEN	Gaia DR2 AEN (mas)
18	BR_excess	Gaia DR2 BP/RP excess factor
19	ur_color	NSC $(u-r)_0$, with Milky Way dust correction applied (mag)
20	rz_color	NSC $(r-z)_0$, with Milky Way dust correction applied (mag)
21	concentration_likelihood	Candidate likelihood based on C_{3-6}
22	proper_motion_likelihood	Candidate likelihood based on proper motion
23	parallax_likelihood	Candidate likelihood based on parallax
24	aen_likelihood	Candidate likelihood based on AEN
25	bre_likelihood	Candidate likelihood based on BR_{excess}
26	color_likelihood	Candidate likelihood based on NSC color
27	total_likelihood	Total likelihood of candidate being a GC in NGC 5128
28	candidate_rank	Classification based on data availability in key data sets; see Table 3
29	confirmed	Is it a confirmed GC in NGC 5128? (y/n)
30	references	Literature references*

*Reference papers: (a) Graham & Phillips (1980), (b) van den Bergh et al. (1981), (c) Hesser et al. (1986), (d) Harris et al. (1992), (e) Holland et al. (1999), (f) Harris et al. (2002), (g) Peng et al. (2004), (h) Martini & Ho (2004), (i) Harris et al. (2004), (j) Woodley et al. (2005), (k) Gómez et al. (2006), (l) Harris et al. (2006), (m) Rejkuba et al. (2007), (n) Woodley et al. (2007), (o) Beasley et al. (2008), (p) Georgiev et al. (2009) (q) Mouhcine et al. (2010), (r) Woodley et al. (2010b), (s) Woodley et al. (2010a), (t) Sinnott et al. (2010), (u) Taylor et al. (2010), (v) Georgiev et al. (2010), (w) Harris et al. (2012), (x) Taylor et al. (2015), (y) Taylor et al. (2017), (z) (V20), (aa) Fahrion et al. (2020), (ab) Müller et al. (2021).
(This table is available in its entirety in FITS format.)

Silver GC candidates have data from PISCeS and either Gaia DR2 or NSC. While the contamination in this set of candidates will be higher than the gold sample, it will also be more sensitive to faint GC candidates. Of the confirmed GCs outside of 10′, 38% have information in two data sets. The silver sample has a total of 13,793 candidates, of which 1750 have *total_likelihood* $\geqslant 0.85$. Between 10′ and 30′ from the center of the galaxy, we find 126 silver GC candidates with *total_likelihood* $\geqslant 0.85$ that have yet to have spectroscopic follow-up or confirmation.

Bronze and copper GC candidates have data only from PISCeS and are absent from both Gaia DR2 and NSC. The likelihood of these candidates is therefore only based on our concentration index measurement C_{3-6} and passing our extended galaxy checks (Sections 4.2 and 4.3). Because there is information available from only one catalog, we raise the minimum C_{3-6} value for the bronze candidates to 2.0, corresponding to a *concentration_likelihood* > 0.977. The bronze sample contains many promising candidates, of which there are 11,860 in total. The remaining 9086 candidates with $1.0 \leqslant C_{3-6} < 2.0$ are placed in the copper sample. These candidates should be treated with caution but may contain true NGC 5128 GCs. For reference, 14% of confirmed GCs outside of 10′ have information only in the PISCeS data set. These groups of candidates are expected to have the most contamination and are somewhat susceptible to the image-level issues apparent in a handful of fields. For instance, a changing FWHM across a Megacam field of view can systematically change the average concentration index value at a small level.

6. Discussion

6.1. GC Spatial Distributions

Our catalog consists of both true GCs and contaminants. To separate these two, and to optimize our catalogs, we assume that the true GCs follow a decreasing power-law function with radius, while the background level is uniform across our survey. We therefore fit our radial density profile of GC candidates using a model with a power law plus uniform background. We first use this model to determine what an appropriate *total_likelihood* threshold is for analyzing the physical properties of GCs in our catalog. Focusing on the gold and silver GC candidates, we examine the total number of candidates above the background, as well as the total number of contaminants at a range of *total_likelihood* thresholds. As

Table 2
Header Information for the Catalog of All PISCeS Sources in NGC 5128

Column	Label	Description
1	ID	Unique "H21" ID
2	Discovery_ID	Discovery ID, if available
3	RA	PISCeS R.A. in decimal degrees (J2000)
4	Dec	PISCeS decl. in decimal degrees (J2000)
5	PISCeS_gmag	PISCeS g-band magnitude (mag)
6	PISCeS_gmag_err	Error of PISCeS g-band magnitude (mag)
7	PISCeS_rmag	PISCeS r-band magnitude (mag)
8	PISCeS_rmag_err	Error of PISCeS r-band magnitude (mag)
9	g_C_3_6	PISCeS g-band concentration index value
10	r_C_3_6	PISCeS r-band concentration index value
11	band_used	PISCeS magnitude band used to calculate *concentration_likeliness*
12	Gaia_RA	Gaia DR2 R.A. in decimal degrees (ICRS)
13	Gaia_Dec	Gaia DR2 decl. in decimal degrees (ICRS)
14	Gaia_Gmag	Gaia DR2 G-band magnitude (mag)
15	pm_ra	Gaia DR2 proper-motion measurement in R.A. direction (mas yr^{-1})
16	pm_ra_err	Error of Gaia DR2 proper-motion measurement in R.A. direction (mas yr^{-1})
17	pm_dec	Gaia DR2 proper-motion measurement in decl. direction (mas yr^{-1})
18	pm_dec_err	Error of Gaia DR2 proper-motion measurement in decl. direction (mas yr^{-1})
19	parallax	Gaia DR2 parallax measurement (mas)
20	parallax_err	Error in Gaia DR2 parallax measurement (mas)
21	AEN	Gaia DR2 AEN (mas)
22	BR_excess	Gaia DR2 BP/RP excess factor
23	NSC_umag	NSC u-band magnitude (mag)
24	NSC_umag_err	Error of NSC u-band magnitude (mag)
25	NSC_gmag	NSC g-band magnitude (mag)
26	NSC_gmag_err	Error of NSC g-band magnitude (mag)
27	NSC_rmag	NSC r-band magnitude (mag)
28	NSC_rmag_err	Error of NSC r-band magnitude (mag)
29	NSC_imag	NSC i-band magnitude (mag)
30	NSC_imag_err	Error of NSC i-band magnitude (mag)
31	NSC_zmag	NSC z-band magnitude (mag)
32	NSC_zmag_err	Error of NSC z-band magnitude (mag)
33	ur_color	NSC $(u-r)_0$, with Milky Way dust correction applied (mag)
34	rz_color	NSC $(r-z)_0$, with Milky Way dust correction applied (mag)
35	concentration_likelihood	Candidate likelihood based on C_{3-6}
36	structure_check	Galaxy/blend check
37	proper_motion_likelihood	Candidate likelihood based on proper motion
38	parallax_likelihood	Candidate likelihood based on parallax
39	aen_likelihood	Candidate likelihood based on AEN
40	bre_likelihood	Candidate likelihood based on BR_{excess}
41	color_likelihood	Candidate likelihood based on NSC color
42	total_likelihood	Total likelihood of candidate being a GC in NGC 5128
43	candidate_rank	Classification based on data availability in key data sets; see Section 3
44	confirmed	Is it a confirmed GC in NGC 5128? (y/n)
45	references	Literature references*

*Reference papers: See Table 1.
(This table is available in its entirety in FITS format.)

shown in Figure 6, we find that using a threshold of *total_likelihood* $\geqslant 0.85$ nearly maximizes the number of GC candidates above the background, while minimizing the number of contaminants. Therefore, for this section, we focus our analysis on the gold and silver GC candidates that have *total_likelihood* $\geqslant 0.85$.

We break down the radial distributions of our combined gold and silver GC candidate population, as well as the gold-only GC candidate population in Figure 7, where both populations have *total_likelihood* $\geqslant 0.85$. Each radial bin contains a constant number of GC candidates: 100 GC candidates for the combined gold and silver population, with 32 entries in the final bin, and 40 GC candidates for the gold-only population, with seven entries in the final bin. The power-law fit to the radial distribution of the gold GC candidate population is given by

$$\rho_g = 0.00141 + 63.7r^{-2.66\pm0.30}, \quad (3)$$

and the fit to the distribution of the combined gold and silver GC candidate population is given by

$$\rho_{g+s} = 0.0277 + 26.6r^{-1.99\pm0.22}, \quad (4)$$

where ρ_g and ρ_{g+s} are GC candidate surface densities in N per square arcminute. These fits are denoted by the curved solid black lines in Figure 7. The combined gold and silver GC candidate population becomes dominated by the background at

Table 3
In Addition to Providing *total_likelihood*, We Identify GC Candidates by a Rank of Gold, Silver, Bronze, or Copper Based on the Amount of Data Available for Each, and Columns (2)–(4) Indicate if the Data Are Available (✓) or Not (×) in the Three Key Data Sets

Candidate Rank	PISCeS	Gaia DR2	NSC	Minimum C_{3-6}	Number of Candidates	
					Total	$\mathscr{L}_{\rm total} > 0.85$
Gold	✓	✓	✓	1.0	5763	181
Silver	✓	✓	×	1.0	13,793	1750
	✓	×	✓	1.0		
Bronze	✓	×	×	2.0	11,860	11,860
Copper	✓	×	×	1.0	9086	8541

Note. For many candidates, there is only one source of information (PISCeS) available, so we label those with $C_{3-6} \geqslant 2.0$ as bronze and those with $1.0 \leqslant C_{3-6} < 2.0$ as copper, where $C_{3-6} = 2.0$ corresponds to *concentration_likelihood* = 0.977 (see Section 4.2). For each rank, the final two columns list the total number of candidates and the number of candidates with *total_likelihood* > 0.85.

a smaller radius (∼1.4 deg; 94 kpc) than the population with only gold candidates (∼1.8 deg; 121 kpc).

The power-law index from the gold sample (-2.66 ± 0.30) is comparable to that found for the radial profile of the GCs in the Milky Way; Bica et al. (2006) found a three-dimensional radial power-law index of −3.9 (corresponding to −2.9 in projected radius) for all clusters beyond 3.5 kpc and an index of −3.6 (−2.6 in projected radius) for the metal-poor clusters that dominate beyond 8 kpc. These values are steeper than typical massive elliptical galaxies, where the projected power-law indices for the full GC systems at large radii are found to range between −1.2 and −2 (Faifer et al. 2011). The index for the combined gold and silver sample (-1.99 ± 0.22) is consistent with the steeper edge of this range. Overall, the spatial profile appears intermediate between massive galaxies and the typical L^*, Milky Way–like galaxy, though it should be revisited once spectroscopy is available.

As a point of comparison, the SCABS catalog GC candidates within 120′, excluding an overdensity at a radius of ∼55′, are fit with a power law of slope −1.22 (T17), shallower than our result. This may partially arise from T17's use of a model that assumes a total population of GCs based on a "known GC" population that contains contamination from foreground stars (see Section 6.3 and Appendix B).

The two-dimensional distribution of our gold and silver GC candidates with *total_likelihood* ⩾ 0.85 is shown in Figure 8. There is a central overdensity, especially along the diagonal from northeast to southwest out to a distance of about 30′ (32.4 kpc), which is angled similarly to the isophotal major axis of the galaxy (35° E of N; Dufour et al. 1979). A majority of the already confirmed GCs in NGC 5128 lie within this radius, though the position angle overdensity seen here has a broader distribution than has been found in previous works. Though we see an overdensity in the one-dimensional GC candidate distribution out to ∼85′, it is less apparent in the two-dimensional distribution. While not plotted, we also see a central (within 40′–50′) enhancement of the bronze candidates above background, consistent with at least some of these being real GCs.

6.2. GC Total Population Estimates

Using a method similar to Harris (2010), we estimate the total size of the GC population in NGC 5128 by forcing a fit to the standard GCLF and estimating the number of GCs below our detection limit. Based on values of $(m-M)_0 = 27.91$ (Harris et al. 2010) and $A_V = 0.35$ (Schlafly & Finkbeiner 2011) and assuming a mean turnover magnitude $M_V = -7.3$ (Harris 2001), the GCLF turnover is expected to occur at $V = 20.95$ mag with $\sigma = 1.4$ mag. We convert our PISCeS *g*- and *r*-band magnitudes to the *V* band using transformation coefficients from Jester et al. (2005).

We split the expected population calculation at a radius of 10′ and assume that within this radius, all bright ($V \leqslant 20.5$ mag) GCs have been found. Outside of 10′, we combine the known confirmed GCs with a sample of our new gold and silver candidate GCs with *total_likelihood* ⩾ 0.85. The sample of GCs is chosen randomly from our candidates to correct for background contamination based on the fits shown in Figure 9. These random samples were chosen 100 times. For both the inner and outer cluster samples, we plot the GCLF and fit a Gaussian function with values discussed above assuming Poisson errors. We also vary the faint-end limit of the fitting range by 0.5 mag and incorporate this into our overall uncertainties.

This method results in a population estimate of 1300 ± 110 GCs, which closely matches the total predicted by Harris (2010). This should be treated as a lower limit, though, since it does not include any GC candidates from the bronze or copper classifications (those that have data only from PISCeS), and it includes only gold and silver clusters with *total_likelihood* ⩾ 0.85. We know that 14% of confirmed GCs outside of 10′ are in the bronze sample, largely due to the incompleteness of Gaia DR2 and NSC at faint magnitudes. Another 4% of confirmed GCs are in the gold and silver sample but have *total_likelihood* < 0.85. Accounting for this incompleteness, we estimate that there are a total of 1450 ± 160 GCs in NGC 5128 within ∼150 kpc.

Forbes (2017) predicted that half of the GC system of an elliptical galaxy will lie within a radius R_e given by $\log R_e = 0.97(\pm 0.4)\log M_* - 9.76(\pm 4.4)$. For a stellar mass of $5.5 \times 10^{11}\ M_\odot$ (Peng et al. 2004), this result predicts that half of NGC 5128's GCs will lie within a radius of 42^{+42}_{-21} kpc. We find that half of our estimated total GC population lies within a radius of 48 ± 3 kpc. Only three GCs beyond this radius have been confirmed, further illustrating the need for spectroscopic confirmation of GCs in the outer halo.

The specific frequency (S_N) of a galaxy is used to measure the relative occurrence of GCs across galaxy types and masses and defined as $S_N = N_{\rm GC} \times 10^{0.4(M_V+15)}$ (Harris & van den Bergh 1981). Using our new GC population estimate of $N_{\rm GC} = 1450$ and an extinction-corrected *V*-band magnitude of $M_V = -21.38$ for NGC 5128 (de Vaucouleurs et al. 1991; Schlafly & Finkbeiner 2011) results in $S_N = 4.1$. This is somewhat higher than other recent S_N calculations for NGC 5128, including $S_N = 2.9$ (T17) and 1.9 (Harris 2010).

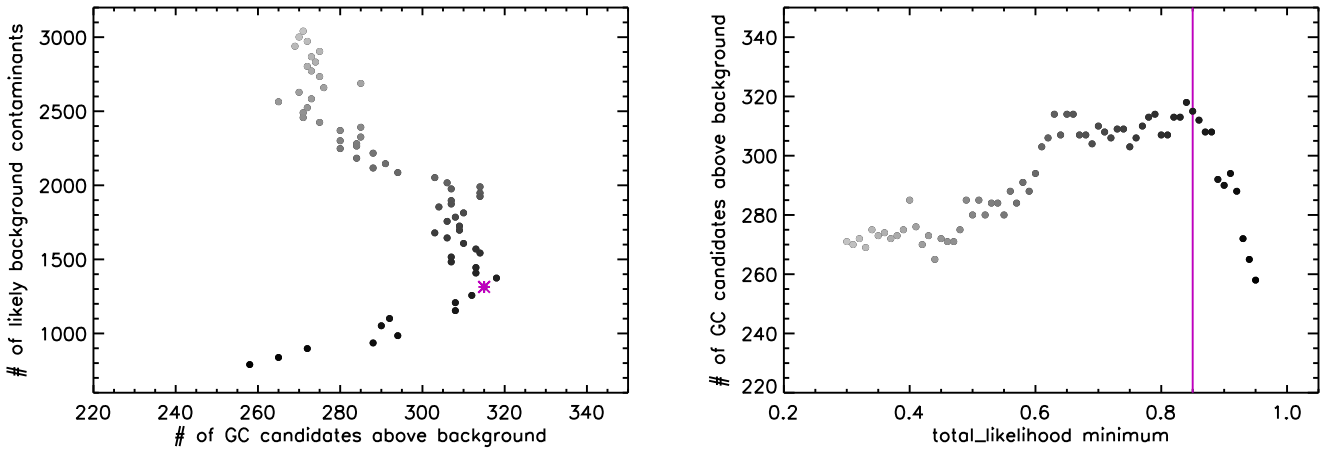

Figure 6. Left: relationship between the number of likely background contaminants and the number of GC candidates above the background level in the gold and silver GC candidate samples with different minimum values of *total_likelihood* between 0.3 and 0.95. The counts are based on power-law fits to the radial distribution of our candidates (e.g., Figure 7). Darker points correspond to a higher minimum *total_likelihood* value. Right: number of GC candidates above the background as a function of minimum *total_likelihood*, where the points are color-coded the same as the left panel. We highlight the gold and silver GC candidates with *total_likelihood* $\geqslant 0.85$ as the most likely to be true GCs based on available information, and this value is indicated with the purple star on the left and the purple line on the right.

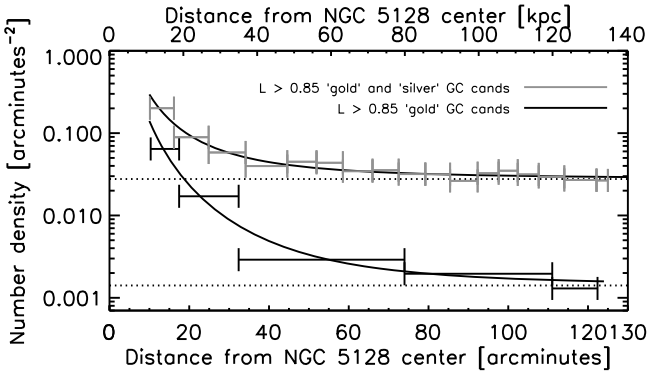

Figure 7. Radial distribution of gold and silver GC candidates with *total_likelihood* $\geqslant 0.85$. Each bin contains 100 GC candidates for the combined gold and silver sample, with 32 entries in the final bin, and 40 GC candidates for the gold-only sample, with seven entries in the final bin. The curved solid black lines mark power-law fits to the GC candidate distributions between 10′ and 125′, given by Equations (3) and (4), and the dotted lines mark the constant background values in the same equations.

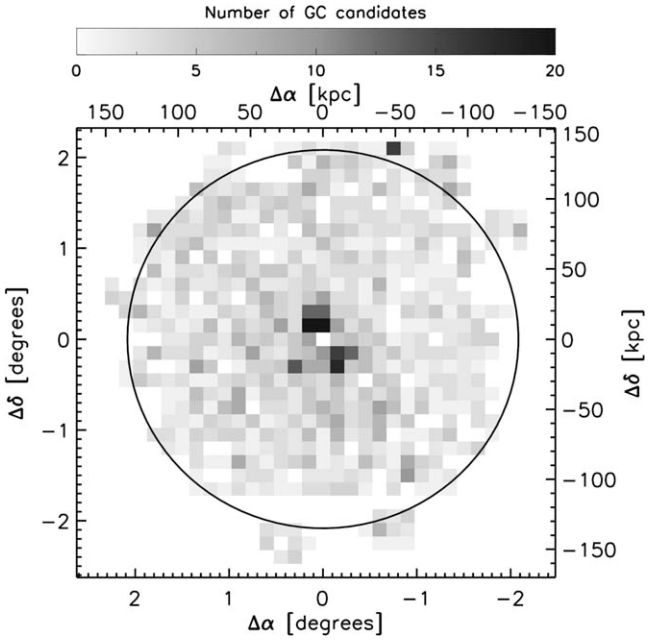

Figure 8. Two-dimensional density distribution of our gold and silver GC candidates with *total_likelihood* $\geqslant 0.85$, where each pixel is $0\overset{\circ}{.}15 \times 0\overset{\circ}{.}15$. The figure is oriented such that north is up and east is left. Note the overdensity of GC candidates close to the center of the galaxy, which is angled similarly to the isophotal major axis of the galaxy (35° E of N; Dufour et al. 1979). We exclude all sources within 10′ from our analysis, leading to a central gap in the GC candidate distribution. The circle marks a distance of 125′ (135 kpc) from the galaxy center, which is about the extent to which PISCeS has full coverage.

These differences are due both to different $N_{\rm GC}$ estimates and to different assumed M_V values.

Our calculation ($S_N = 4.1$) is consistent with the idea of Graham (1979) that NGC 5128 experienced a merger between an elliptical galaxy with a relatively high S_N and a second gas-rich galaxy, which would typically have had a lower S_N.

6.3. Comparison with Previous Results

Cross-matching items in our GC candidate catalog with the fiducial sample of 69 confirmed GCs, we find that 65 are recovered with *total_likelihood* $\geqslant 0.85$ (this is, of course, largely by construction, as we used the fiducial sample to guide our GC candidate selection methodology). The remaining four fiducial sample GCs have positions in color–color space near the border of the color selection ellipse discussed in Section 4.5 and therefore have lower values for their final *total_likelihood* values.

We broaden our comparison sample to include all confirmed GCs; see Appendix A for a list. Comparisons of recovery fractions for the gold, silver, and bronze rank classifications as a function of radius and magnitude are shown in Figure 10; no confirmed GCs belong to the copper rank. The requirement for data from the NSC and Gaia DR2 catalogs causes faint-end completeness to drop in the gold and silver GC candidate populations. We recover a total of 192 out of 198 (97%) confirmed GCs that are outside of 10′ and in PISCeS. Additionally, 155 out of 198 (78%) have *total_likelihood* $\geqslant 0.85$, where 69 GCs are in the gold sample, 56 GCs are in the silver sample, and 30 GCs are in the bronze sample. Those confirmed GCs that are not recovered or have low *total_likelihood* values typically have low concentration index values or were identified

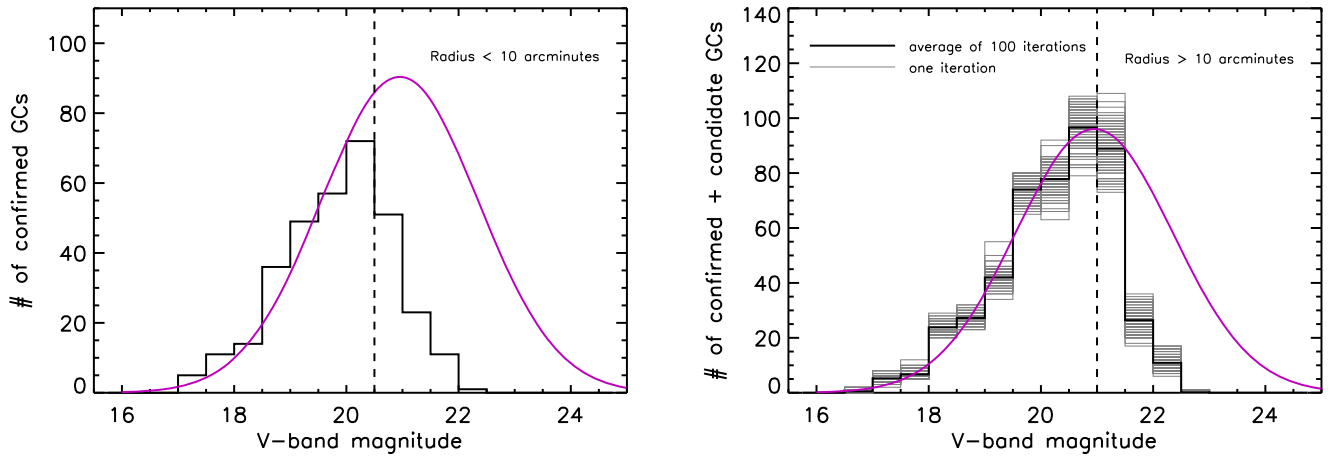

Figure 9. Illustration of our process to calculate the total number of GCs in NGC 5128, using Gaussian functions fitted to the expected GCLF, split at a radius of 10′. The confirmed GC population within 10′ (left) is assumed to be complete for $V \lesssim 20.5$ mag. Outside of 10′ (right), the known population of confirmed GCs is combined with a background-subtracted sample of our gold and silver candidate GCs with *total_likelihood* $\geqslant 0.85$. Plotted here are 100 iterations of this background-corrected candidate sampling (gray) and their average (black). Only data to the left of the dashed vertical lines in both histograms are used in the respective Gaussian fits.

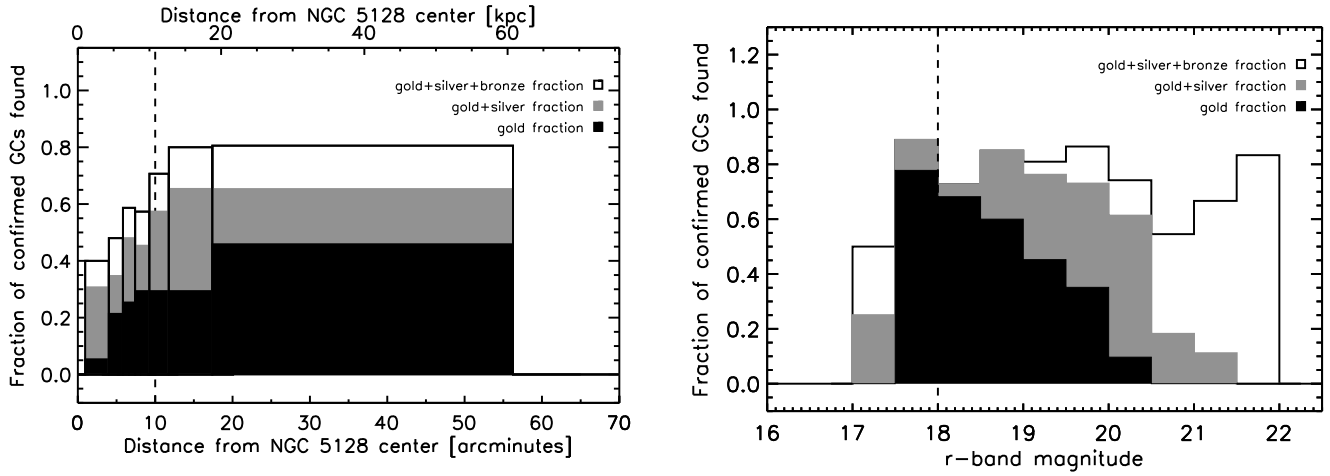

Figure 10. Left: recovery fraction of confirmed GCs with *total_likelihood* $\geqslant 0.85$, binned by sets of 75 with increasing radial distance from the center of NGC 5128. The last bin has 72 GCs. Within 10′ of the galaxy center, our GC selection process is not effective due to crowding. Right: recovery fraction with *total_likelihood* $\geqslant 0.85$ of the confirmed GCs outside of 10′, binned by *r*-band magnitude, without extinction correction applied. The dashed vertical line indicates where Gaia DR2 begins to become incomplete (Gaia Collaboration et al. 2018b), and thus where we expect the gold sample to decrease.

as galaxies due to close proximity to foreground stars. Within 10′, we only recover 53% of the confirmed GCs, due to crowding. Recall that because our methods are tailored to work in the uncrowded regions far from the center of NGC 5128, we exclude the centralmost portion of the galaxy from our catalogs.

We fail to recover a small number of bright GCs/UCDs, mostly due to saturation of the PISCeS data but also because of our cuts on structure that identify background galaxies. This is why we developed a focused approach in V20 to obtain a complete sample of the brightest GCs, including cluster candidates lying outside the PISCeS footprint. Of the 480 candidates from V20 that lie within the PISCeS footprint, only 102 are also included in our catalog.

Apart from V20, the only other catalog presenting GC candidates at comparably large radii is the SCABS catalog from T17. We find that 864 of the 2087 GC candidates from SCABS that are in the PISCeS footprint are recovered as candidates by our tests, and 511 have *total_likelihood* $\geqslant 0.85$ in our catalog. An additional ≈1100 SCABS GC candidates are outside of the PISCeS footprint or within 10′ of the center of the galaxy and so are not included in our catalog. Of the ≈1450 SCABS candidates with *total_likelihood* < 0.85 in our catalog, 67% are found to have stellar-like concentration index values in our PISCeS data, and 37% have high-confidence parallax or proper-motion measurements in Gaia DR2. This suggests that the catalog has a high contamination rate, and that the PISCeS concentration information provides valuable complementary data to the colors used in the SCABS candidate selection. Additionally, SCABS recovered only 251 out of their sample of 643 "confirmed" GCs.[12] Before their final step of deriving GC candidate likelihoods based on color, however, they reported that they successfully recovered ∼90% of confirmed GCs. This low recovery rate in the final step appears to be caused by their method of modeling the ratio of stars to GCs,

[12] The sample of "confirmed" GCs used by T17 is not the same as what we list in Appendix A. They did not provide a list of the confirmed GCs that they used to assess their GC candidate selection technique, and they cited private communication as a source. Their sample likely includes contamination from foreground stars; see Appendix B.

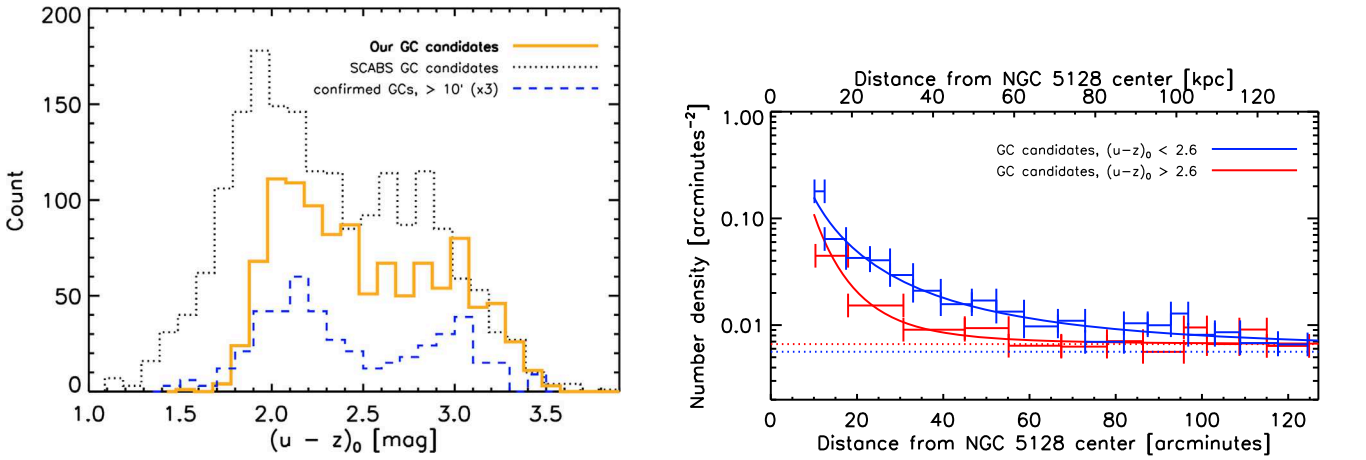

Figure 11. Distributions of gold and silver GC candidates with NSC photometric data and *total_likelihood* $\geqslant 0.85$. In the left panel, the bimodal shape of our GC candidate color distribution closely matches that of the confirmed GCs outside of 10′ from the center of the galaxy, which is multiplied by 3 to more clearly show its shape. There is an offset between the color of our GC candidates and those found with the methods employed by T17. The NSC photometry has been dust-corrected. Right: radial distribution of GC candidates, split based on color with a critical value of $(u-z)_0 = 2.6$ mag. Each radial bin contains 30 GC candidates, with 20 in the final blue bin and 28 in the final red bin. The curved solid lines mark the power-law fits to the GC candidate distributions between 10′ and 125′, given by Equations (5) and (6), and the dotted lines mark the constant background values in the same equations.

which is controlled by an expected population size. Additionally, T17 predicted a total of ∼1100 GCs within a projected 55 kpc from the center of NGC 5128 and ≈3200 GCs within ∼140 kpc. This is more than double our prediction for the total number of GCs in the galaxy (Section 6.2).

6.4. Color Bimodality

In many galaxies, the population of GCs is observed to have a distinctly bimodal metallicity distribution; though most GCs are metal-poor, the "blue" GCs in a given galaxy are, on average, more metal-poor, and the "red" GCs are, on average, more metal-rich (e.g., Brodie & Strader 2006 for a review). The difference may be the result of dual halo mode formation, where metal-rich GCs form in massive progenitors and metal-poor GCs form in low-mass satellite galaxies that are later accreted as part of hierarchical galaxy formation (e.g., Park & Lee 2013; Lee & Jang 2016; Forbes & Remus 2018; El-Badry et al. 2019). This bimodality is one of the most studied properties of GC systems, since these subpopulations show differences in their intrinsic characteristics, such as their spatial distribution and kinematics.

As expected, there is a bimodal color distribution of our gold and silver GC candidates with *total_likelihood* $\geqslant 0.85$. Figure 11 shows the distribution in NSC $(u-z)_0$ color space of these candidates. The right and left edges of our candidate color distribution match the distribution of the confirmed GCs that have NSC data and are outside of 10′, which has been multiplied by a factor of 3 to show the distribution's shape. This match between the color ranges of our candidates and the confirmed GCs is largely by construction, as we used a subset of confirmed GCs to guide the color selection step in our GC candidate selection process (Section 4.5).

We also plot the NSC color of the SCABS GC candidates from T17. The offset in the color distributions between the SCABS GC candidates and the confirmed GCs may arise because of the high rate of contamination in the SCABS sample, as discussed in Section 6.3.

The radial distributions of the same gold and silver GC candidates are plotted in Figure 11, where GC candidates with $(u-z)_0 < 2.6$ are in the blue sample and GC candidates with $(u-z)_0 > 2.6$ are in the red sample. The power-law fit to the radial distribution of the blue GC candidates is given by

$$\rho_b = 0.00562 + 9.72r^{-1.81\pm0.23}, \quad (5)$$

and the fit to the radial distribution of the red GC candidates is given by

$$\rho_r = 0.00664 + 79.3r^{-2.89\pm0.64}. \quad (6)$$

The slope obtained for the red subpopulation is steeper than the ones obtained for the blue subpopulation and the entire gold and silver GC candidate system (Equation (4)), as it is more concentrated toward the center. This follows what has been observed for many galaxies (e.g., Brodie & Strader 2006; Faifer et al. 2011; Forbes et al. 2012). At all radii that are include in the fit, there are more blue than red GCs, further indicating that NGC 5128 has a rich merger history (e.g., Peng et al. 2004; Beasley et al. 2008).

6.5. Milky Way Foreground Star Contamination

Because of the relative proximity of NGC 5128 to the Galactic disk, there is significant contamination from foreground stars. We find that nearly all of the objects that lie within the magnitude range expected for NGC 5128 GCs are actually Galactic foreground stars. Unfortunately, removing all of the foreground star contamination from GC catalogs is very tricky. Of the 630 GCs identified in previous studies, 355 have both a measured radial velocity and information in Gaia DR2. A histogram of the radial velocities of these GCs is plotted in Figure 12. Overlaid in blue, we show the 50 objects that have nonzero proper-motion and/or parallax measurements with a confidence of 3σ or greater. These objects are contaminant foreground stars with high velocities, not GCs in NGC 5128 as previously thought, and are listed and discussed further in Appendix B.

We estimate that up to ≈80% of entries with gold or silver rank and *total_likelihood* $\geqslant 0.85$ and ≈42% of entries with gold rank and *total_likelihood* $\geqslant 0.85$ are not true GCs in NGC 5128, based upon the density of the background in the fit to the radial distribution of candidates, shown in Figure 7. We

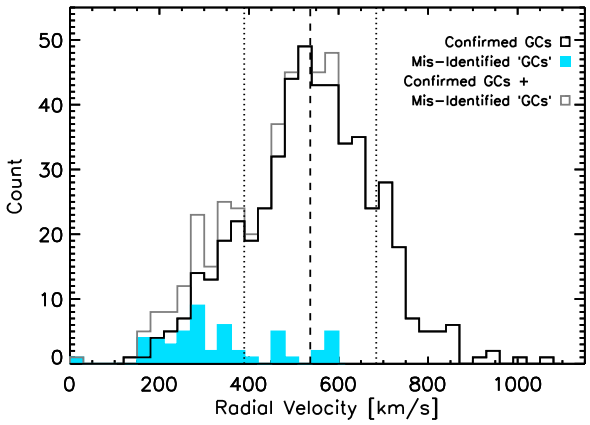

Figure 12. Histogram of 507 confirmed GCs with radial velocity measurements. The dashed line marks the newly measured mean radial velocity value of 537 km s^{-1}, and the dotted lines mark $\pm 1\sigma$, where $\sigma = 148$ km s^{-1}. The standard critical radial velocity for GC confirmation in NGC 5128 is 250 km s^{-1}. Targets with velocities below this value were typically confirmed via structural parameters or visual resolution into component stars from HST images. The filled blue histogram shows the 50 objects that were identified by a past NGC 5128 survey as "GCs" that have nonzero proper-motion measurements in Gaia DR2 of 3σ or greater. These misidentified "GCs" are actually Milky Way foreground stars and are listed and discussed further in Appendix B.1. By removing these contaminants, the distribution of radial velocities becomes more symmetric about the mean value.

expect this percentage to be dependent on the radial distance from the center of the galaxy and the amount of information available for the candidates.

6.6. Velocity Dispersion of GCs around NGC 5128

The systematic velocity of NGC 5128 is 541 km s^{-1} (Hui et al. 1995) with a velocity dispersion of $\sigma \sim 150$ km s^{-1} (Wilkinson et al. 1986; Silge et al. 2005). Based on a sample of 605 identified GCs, Woodley et al. (2010a) calculated a mean GC radial velocity of 517 ± 7 km s^{-1} with $\sigma = 160 \pm 5$ km s^{-1}. They noted that because this value is lower than the accepted systematic velocity of the galaxy, their catalog may be contaminated on the low-velocity end. We have found and removed contaminant foreground stars from the confirmed GC population (see Appendix B) and redone the calculation. Of the cleaned list of confirmed GCs (see Table 4 in Appendix A), 507 have radial velocity measurements, with a mean radial velocity of 537 km s^{-1} and $\sigma = 148$ km s^{-1}. Figure 12 shows radial velocity histograms for the cleaned list of confirmed GCs, the contaminant Milky Way foreground stars that were previously misidentified as GCs, and the combination of these two populations. Removing the contaminant foreground stars makes the distribution of the GC radial velocity measurements more symmetric about the mean value and brings the mean velocity measurement of the GC system closer in line with that of the galaxy as a whole, as seen in other galaxies (e.g., Pota et al. 2015). We defer a thorough kinematic and dynamical analysis to a future paper that will also incorporate new radial velocities.

6.7. Future Work

Now that we have a new catalog of NGC 5128 candidate GCs out to ∼150 kpc, further observations are required to confirm which are true GCs in NGC 5128. We have begun taking spectroscopic observations to measure candidate GC radial velocities using Magellan/Megacam, AAT/2DF, and SOAR. For brighter GCs, we will also be able to estimate metallicities, providing further information on NGC 5128's accreting substructures. The results will be published in an upcoming paper.

Once we have a larger population of confirmed GCs at large radii, we will be able to identify specific GCs that are associated with streams and shells around NGC 5128, similar to the work done for M31 (Veljanoski et al. 2014; Mackey et al. 2019). The kinematics of GCs associated with NGC 5128's streams and shells will provide important constraints on the accreted systems' orbit, mass, and concentration, while the velocity dispersion, number, and color of the nonassociated GCs can provide complementary constraints on the host galaxy mass. It is also possible that many of NGC 5128's past merger/accretion events may not have visible remnants in the PISCeS RGB map but could be detectable kinematically via its GCs. Additionally, by using GCs at larger radii, we will be able to calculate the galaxy's enclosed mass at a larger radius.

The release of Gaia Early Data Release 3 and the upcoming full Gaia Data Release 3 include information on additional targets around NGC 5128, to a fainter limiting magnitude of $G \approx 21$, and with higher-precision proper-motion and parallax measurements than Gaia DR2 (Gaia Collaboration et al. 2021). This will allow for the removal of additional contaminant foreground stars from the silver, bronze, and copper GC candidate categories and a more confident *total_likelihood* score that takes into account the structural parameters (e.g., AEN and BR_{excess}) given to those candidates that now have Gaia data available for them.

7. Summary

We present a new technique for identifying GCs in the Local Volume using a combination of ground- and space-based observations. We combine data from Gaia DR2 with the ground-based PISCeS and NSC data sets to select 40,502 GC candidates in NGC 5128 out to a projected radius of ∼150 kpc, as presented in Table 1. We highlight the 1931 candidates in the gold and silver rank with *total_likelihood* $\geqslant 0.85$ as the most likely to be true GCs in NGC 5128 and therefore the most promising targets for follow-up spectroscopic confirmation.

Our GC candidate selection process identifies extended objects using a concentration index versus magnitude relationship and then rejects foreground star and background galaxy contaminants based on astrometric motion and structural parameters from Gaia DR2 and color from NSC. To assist in selecting extended objects, we provide 3σ confidence lines in Gaia AEN and BR_{excess} versus G-mag space and a color selection ellipse in NSC $(u-r)_0$ versus $(r-z)_0$ space. Each GC candidate in our catalog has a *total_likelihood* value between zero and 1 (where numbers closer to 1 represent a larger chance that the source is a GC), as well as a gold, silver, bronze, or copper rank (to indicate the amount of information available). Our selection technique recovers 155 out of 198 (78%) confirmed GCs that are outside of 10′ and in PISCeS with a *total_likelihood* $\geqslant 0.85$.

Our sample of gold and silver GC candidates exhibits a clear central overdensity. The one-dimensional radial distributions of the gold and combined gold and silver GC candidate populations can be fit by power laws with exponents of −2.66 and −2.01, respectively. Using the expected parameters to fit a GCLF to the combined confirmed and candidate

samples, we estimate that there are a total of 1450 ± 160 GCs in NGC 5128 within ∼150 kpc and that half of the GCs lie within a radius of 48 ± 3 kpc.

Our GC candidates exhibit a bimodal color distribution matching that of the confirmed GCs outside of 10′. The metal-rich subpopulation is more centrally concentrated, with a power-law exponent of ∼−2.9, though the metal-poor subpopulation, with a power-law exponent of ∼−1.8, is larger at almost all radii.

We cull contaminant objects from the list of known confirmed GCs and provide an updated mean radial velocity for confirmed GCs of 537 km s^{-1} with $\sigma = 148$ km s^{-1}, which is closer in line with the values for the galaxy as a whole. The cleaned list of confirmed GCs can be found in Table 4.

Once GCs at large radii have been confirmed, we will be able to identify those that are associated with streams and shells around NGC 5128, providing information about the accreted systems and host galaxy, as has been done in M31 (Veljanoski et al. 2014; Mackey et al. 2019). We will additionally apply these techniques combining Gaia with ground-based observing to identify slightly extended GCs in further galaxies in the Local Volume.

This research uses services or data provided by the NOAO Data Lab. The NOAO is operated by the Association of Universities for Research in Astronomy (AURA), Inc., under a cooperative agreement with the National Science Foundation.

This work has made use of data from the European Space Agency (ESA) mission Gaia (https://www.cosmos.esa.int/gaia), processed by the Gaia Data Processing and Analysis Consortium (DPAC; https://www.cosmos.esa.int/web/gaia/dpac/consortium). Funding for the DPAC has been provided by national institutions, in particular the institutions participating in the Gaia Multilateral Agreement.

A.K.H. and D.J.S. acknowledge support from NSF grants AST-1821967 and 1813708. A.C.S. acknowledges support from NSF grant AST-1813609. J.S. acknowledges support from NSF grants AST-1514763 and AST-1812856 and the Packard Foundation. J.D.S. acknowledges support from NSF grant AST-1412792. Research by D.C. is supported by NSF grant AST-1814208.

We thank Pauline Barmby for supplying globular cluster structural properties from McLaughlin et al. (2008).

Lastly, we thank the anonymous reviewer, whose comments and suggestions helped improve and clarify this manuscript.

Facilities: Magellan:Clay (Megacam), Gaia.

Software: `SExtractor` (Bertin & Arnouts 1996), SWarp (Bertin 2010), the IDL Astronomy User's Library (Landsman 1993).

Appendix A
Table of Confirmed GCs

Based upon new observations and data, we can show that only 557 of the 630 objects that have been identified as NGC 5128 GCs in the literature are genuine confirmations. In this appendix, we present a cleaned catalog of GCs in NGC 5128. We also provide additional notes on objects that we have "demoted."

It has been nearly a decade since an up-to-date comprehensive catalog of confirmed GCs around NGC 5128 was published. Recent papers have either studied a subset of candidates and known GCs or relied on "private communication" as one of their data sources. With decades of observations and a multitude of naming conventions and selection criteria, we hope to aid in future studies by providing information about all confirmed GCs known at this time in a clear way.

We present a compilation catalog of the 557 confirmed GCs around NGC 5128. The most common way to confirm that a candidate GC is associated with NGC 5128 is to measure its radial velocity, since most GCs at that distance are too small to visually resolve into component stars with ground-based data. The galaxy NGC 5128 has a systematic velocity of 541 km s^{-1} (Hui et al. 1995) and a central stellar velocity dispersion of ∼150 km s^{-1} (Wilkinson et al. 1986). Therefore, to avoid contamination from Milky Way foreground stars, past surveys have considered a GC to be confirmed if its radial velocity is greater than 250 km s^{-1}. Three studies confirm select GCs based on morphological parameters if their radial velocity

Table 4
Confirmed GCs around NGC 5128

ID (H21)	Discovery ID	References*	R.A. (J2000)	Decl. (J2000)	Radial Distance (arcmin)	g (mag)	r (mag)	v_r (km s^{-1})	v_r Reference	Notes
H21-069900	Fluffy	z	199.545349	−44.157249	103.8	19.42	18.73	719 ± 6	z	
H21-154980	KK197-01	p, aa	200.499166	−42.535139	48.37			636 ± 16	aa	
H21-156130	KK197-03	p, aa	200.510634	−42.536913	47.90	21.41	20.75	642 ± 3	aa	
H21-159794	H12-556	w, y, v	200.552063	−42.753072	39.41	21.29	20.63			
H21-160341	KKs55-02	ab	200.557787	−42.734733	39.66			531 ± 15	ab	
H21-183480	KV19-212	z	200.790878	−43.874443	56.25	18.28	17.53	535 ± 2	z	1
H21-194226	32	i, k, n, o, y	200.909700	−42.773027	25.31	18.86	18.22	497 ± 33	o	1
H21-195812	C40	f, g, i, k, n, o, y	200.926424	−43.160459	20.56	19.37	18.64	443 ± 48	o	
H21-196535	VHH81-01	b, c, g, i, n, o, r, s, x, y	200.934075	−43.186591	20.89	18.12	17.38	645 ± 10	s	3
H21-196891	GC0563	r, y	200.937603	−43.019830	18.65	19.67	18.85	533 ± 35	r	1

*See Table 1 for annotation references. (1) The GC is in our fiducial sample (see Section 3). (2) The position of GC pff-gc-028 was originally listed in Peng et al. (2004) in HMS coordinates as 13:25:01.16, −42:56:51.05. In their Table 1, Woodley et al. (2007) gave the position of this GC as 13:20:01.16, –42:56:51.05, which, due to an unfortunate change in one digit of R.A. minutes, points to an empty patch of sky. (3) The position of C01/GC0005 is listed in Taylor et al. (2010) as 200.93333, –43.187083, which is 2.″65 away from the position indicated by all other studies that noted this GC.

(This table is available in its entirety in machine-readable form.)

measurement is below this critical value (Mouhcine et al. 2010; Woodley et al. 2010a, 2010b). Additionally, Harris et al. (2002, 2006) listed new GCs found via their resolved stellar outskirts in HST Space Telescope Imaging Spectrograph and Advanced Camera for Surveys (ACS) imaging, respectively, and some of these GCs do not currently have radial velocity measurements. We consider all of these "confirmed" GCs of NGC 5128, unless there exists evidence to the contrary.

For each confirmed GC around NGC 5128, Table 4 first lists the ID from the GC candidate catalog in this paper, the discovery ID, and all references in the literature. Also listed are the R.A. and decl. in degrees (J2000), as well as the *g*- and *r*-band magnitudes. These measurements are from the PISCeS data set to provide uniform astrometric and photometric systems, and the magnitudes have not been extinction-corrected. Next, we include the most recently published radial velocity and error (kilometers per second), along with its reference. In the final column, we note which GCs are in our fiducial sample (Section 3) and two GCs that have slightly incorrect positions in follow-up surveys. For completeness, if a GC is not in PISCeS or is within 10′ from the center of NGC 5128, we still include it in this catalog using its most recent astrometry and without PISCeS photometry.

Appendix B
Misclassified Objects

In building a catalog of known GCs around NGC 5128, it is important to note instances of 73 targets that have been erroneously confirmed as GCs. We find 50 targets that we reclassify as foreground stars based on Gaia DR2 proper-motion and/or parallax measurements. These are discussed in Appendix B.1 and listed in Table 5. Additionally, there are also 32 occurrences in which follow-up measurements of velocity, spectra, or structure do not agree with a target's initial classification (of which an additional 23 are objects that have been reclassified as foreground stars). These are discussed in Appendix B.2 and listed in Table 6.

There is one additional case in which the position listed for an identified GC points to an empty patch of sky that cannot be readily matched with a nearby known or candidate GC. The position for GC 0472 from Woodley et al. (2010b) is given as $\alpha = 201.^{\circ}42908$, $\delta = -43.^{\circ}00056$. This is only 3.′6 from the center of NGC 5128, a region crowded with stars and dust. The position could refer to a source at $\alpha = 201.^{\circ}42822$, $\delta = -43.^{\circ}00056$ (a distance of 2.″3 away), but we do not want to make that assumption here, as no other NGC 5128 GC surveys have published observations of this object. We note that there is a very good match between the astrometry used in Woodley et al. (2010b) and the PISCeS data used here, so this mismatch is unique.

B.1. Foreground Stars with Measured Proper Motions in Gaia DR2

With the modest systematic velocity and velocity dispersion of NGC 5128, there is some overlap in the radial velocity measurements of NGC 5128 GCs and Milky Way foreground stars; a radial velocity measurement greater than 250 km s^{-1} alone cannot definitively give membership for every object. Of the ≃600 identified GCs in NGC 5128, 355 can also be found in Gaia DR2, and 50 of these have a recorded proper motion and/or parallax with a significance greater than 3σ. Their velocities are plotted as the blue histogram in Figure 12. Because these objects have high-confidence apparent-motion measurements, we can infer that they are Galactic foreground stars, rather than GCs in NGC 5128. These foreground stars can also be seen as distinct from the fiducial sample GCs in AEN–magnitude and BR_{excess}–magnitude space, as seen by the blue diamonds in Figure 4, showing that all of these objects match better to Gaia's standard astrometric model of a star than our fiducial sample of confirmed GCs does. Five of these stars also have HST imaging and do not have the characteristic resolved stellar outskirts of true GCs. The stars with $\gtrsim$500 km s^{-1} radial velocities are possibly being ejected from the Milky Way, although the uncertainties on many of these measurements are relatively large (≈100–200 km s^{-1}) and so warrant further observations.

For each foreground star that was previously thought to be a GC in NGC 5128, Table 5 first lists the R.A. and decl. in degrees (J2000). The position measurements are all from the PISCeS data set to provide a uniform astrometric system. Next, we list the most recent reported radial velocity and error (kilometers per second), along with its reference. Columns (5)–(7) list the R.A. proper motion and error (milliarcseconds per year), the decl. proper motion and error (milliarcseconds per year), and the parallax motion and error (milliarcseconds per year) from Gaia DR2. Finally, we include the various names each has had in the literature, along with references. In the list of names, we give preference to the earliest naming convention when small differences are found, such as the removal or addition of preceding zeros or the removal, addition, or slight alteration of prefixes.

We identified two authentic GCs that have high apparent-motion measurements in Gaia DR2 (see notes 10 and 18 in Table 6). Because Gaia DR2 is designed to observe stars in the Milky Way, it does not always provide accurate measurements of sources that are extended or in very crowded regions. We urge caution and follow-up observations of the objects in Table 5, especially those within 10′ of the center of NGC 5128.

B.2. Conflicting Measurements

Thirty-two of the identified GCs in NGC 5128 have conflicting classifications in the literature. A majority of these conflicting classifications occur because the target was measured to have a radial velocity within the standard acceptable range of ≈250–1000 km s^{-1} by one group but outside this range by another. Additionally, two objects were identified as GCs based on their radial velocities but later found to be stars based on HST/ACS imaging (see note 9 in Table 6). Another object was subsequently identified as a star because of its spectrum (see note 5 in Table 6). These objects with conflicting measurements have been matched between studies based on position and, in many cases, by their ID as well. When examining these objects with PISCeS data, several of them can be visually identified as background galaxies. We believe seven of these objects are indeed true GCs because a majority of their measurements classify them as such and they do not visually look like galaxies; thus, they are included in Table 4.

For each object with conflicting measurements, Table 6 first lists the R.A. and decl. in degrees (J2000). The position measurements are from the PISCeS data set to provide a uniform astrometric system. Next, we list the conflicting radial velocities and errors (kilometers per second) along with their

Table 5
Foreground Stars that Were Previously Misclassified as GCs

R.A. (deg J2000)	Decl. (deg J2000)	v_r (km s^{-1})	v_r References*	μ_α (mas yr^{-1})	μ_δ (mas yr^{-1})	ϖ (mas yr^{-1})	Names*	Notes
200.858796	−42.924206	235 ± 43	r	−4.81 ± 0.42	−0.79 ± 0.35	0.73 ± 0.26	GC0560[r]; T17-0955[y]	
200.867666	−42.795083	181 ± 68	r	−8.67 ± 0.16	−0.08 ± 0.13	0.27 ± 0.09	GC0561[r]; T17-0962[y]	
200.868472	−42.886790	238 ± 26	r	−4.86 ± 0.49	−3.69 ± 0.40	0.44 ± 0.30	GC0562[r]; T17-0964[y]	
200.977151	−43.333608	274 ± 49	r	−8.72 ± 1.59	0.51 ± 1.14	−0.10 ± 0.74	GC0007[n,r]; AAT301956[o]; T17-1035[y]	
200.994011	−42.954703	590 ± 144	r	−11.7 ± 0.99	−0.34 ± 0.74	0.44 ± 0.57	GC0009[n,r]; AAT101931[o]; T17-1048[y]	
200.998369	−42.922017	293 ± 83	o	−3.35 ± 1.03	0.28 ± 0.82	−1.03 ± 0.61	GC0012[n]; AAT102120[o]; T17-1054[y]	
201.024844	−43.065200	277 ± 67	o	−6.15 ± 1.09	−8.05 ± 0.86	−0.24 ± 0.72	GC0016[n]; AAT103195[o]; T17-1068[y]	
201.027472	−42.882931	285 ± 29	r	−9.81 ± 0.35	−2.19 ± 0.31	0.19 ± 0.23	GC0565[r]; T17-1071[y]	
201.035905	−43.274189	305 ± 56	n	6.09 ± 1.01	−5.08 ± 0.73	0.72 ± 0.63	GC0017[n]; T17-1081[y]	
201.040767	−42.748422	173 ± 117	r	−6.87 ± 0.46	−2.66 ± 0.30	0.49 ± 0.21	GC0566[r]; T17-1084[y]	
201.137766	−43.312476	344 ± 58	n	−2.96 ± 0.96	−4.63 ± 0.83	1.60 ± 0.56	pff-gc-010[g,i,l]; GC0035[n]; T17-1180[y]	1
201.181460	−43.145317	465 ± 38	o	−4.66 ± 0.52	−1.55 ± 0.43	−0.13 ± 0.32	GC0047[n,u]; AAT109380[o]; T17-1216[y]	
201.199229	−43.145415	353 ± 29	r	−3.25 ± 1.40	−3.98 ± 1.14	−1.07 ± 0.88	GC0575[r,u]; T17-1240[y]	
201.216990	−43.075755	195 ± 29	q	−6.81 ± 1.24	−2.84 ± 0.88	−0.19 ± 0.64	C100[f,q]; GC0068[n,r,u]; T17-1269[y]	
201.220601	−43.198898	302 ± 166	o	−10.1 ± 1.39	−6.18 ± 1.23	0.07 ± 0.92	GC0069[n]; AAT111033[o]; T17-1270[y]	
201.224941	−43.073484	466 ± 87	o	−5.11 ± 1.08	−7.67 ± 0.84	−0.78 ± 0.59	GC0071[n,u,x]; AAT111185[o]; T17-1278[y]	
201.228369	−43.147004	197 ± 29	r	−12.9 ± 0.71	−3.60 ± 0.58	0.74 ± 0.43	GC0577[r,u]; T17-1289[y]	
201.235562	−42.658724	158 ± 50	r	0.14 ± 0.36	−2.75 ± 0.28	0.78 ± 0.16	GC0579[r]; T17-1306[y]	
201.237909	−42.648595	170 ± 45	r	−1.41 ± 0.54	−1.61 ± 0.40	0.08 ± 0.23	GC0580[r]; T17-1311[y]	
201.269183	−43.122730	456 ± 118	o	1.89 ± 0.78	−4.51 ± 0.72	0.67 ± 0.47	GC0118[n,u]; AAT112964[o]; T17-1385[y]	
201.287915	−42.400245	456 ± 52	o	−3.57 ± 0.52	−3.26 ± 0.57	0.03 ± 0.28	pff-gc-039[g,i,o]; GC0133[n]; T17-1422[y]	
201.292702	−42.919294	576 ± 12	r	1.11 ± 1.14	−1.43 ± 1.02	−2.24 ± 0.69	GC0137[n,r,u]; K-033[o,q]; T17-1429[y]	
201.296247	−42.967546	330 ± 61	o	0.09 ± 0.62	−14.0 ± 0.48	0.18 ± 0.32	HGHH-G348[d,g,i,o]; GC0142[n,u]; T17-1437[y]	
201.308075	−42.961843	373 ± 36	o	−8.33 ± 0.51	−0.37 ± 0.42	0.09 ± 0.27	HGHH-G271[d,g,i,j,o]; GC0155[n,u]; T17-1464[y]	
201.311756	−43.686271	502 ± 53	o	−4.20 ± 0.65	1.67 ± 0.49	0.65 ± 0.31	pff-gc-046[g,i,o]; GC0159[n]; T17-1472[y]	
201.318460	−43.059162	352 ± 136	n	−8.97 ± 1.81	−2.93 ± 2.38	−0.01 ± 1.07	AAT114993[l]; GC0170[n,u]; T17-1487[y]	1
201.329612	−43.201107	453 ± 232	o	−18.9 ± 1.11	−1.72 ± 0.93	0.56 ± 0.61	GC0183[n]; AAT320656[o]; T17-1515[y]	
201.339502	−43.324865	163 ± 57	r	−25.6 ± 1.14	−2.48 ± 0.85	0.62 ± 0.72	GC0427[r]; T17-1533[y]	
201.357052	−42.627947	404 ± 74	o	−16.7 ± 1.33	2.30 ± 1.14	1.72 ± 0.53	GC0198[n]; AAT204119[o]; T17-1557[y]	
201.358160	−43.057139	269 ± 27	q	−8.33 ± 0.73	−0.81 ± 0.73	0.40 ± 0.42	HGHH-46[d,g,i,o]; GC0200[n,u]; GC0462[q]; T17-1560[y]; T17-1561[y]	2
201.358752	−43.189572	243 ± 19	r	−5.34 ± 0.41	−2.25 ± 0.38	−0.19 ± 0.27	GC0519[r]; T17-1562[y]	
201.370066	−43.072667	553 ± 155	r	−4.23 ± 0.32	−2.76 ± 0.31	0.16 ± 0.20	C145[l]; GC0207[n,r,u]; T17-1578[y]	3
201.376149	−43.698210	297 ± 40	n	−2.61 ± 1.64	−5.08 ± 1.23	−0.96 ± 0.77	pff-gc-054[g]; GC0216[n]; T17-1593[y]	
201.394333	−43.054556	585 ± 97	r	−6.55 ± 0.29	0.44 ± 0.27	0.31 ± 0.18	C152[l]; GC0241[n,r]; T17-1634[y]	3
201.396764	−43.200422	243 ± 61	n	−12.3 ± 0.73	1.40 ± 0.57	0.27 ± 0.33	58[i]; WHH-21[j]; GC0247[n]; T17-1644[y]	
201.408318	−43.283137	257 ± 59	o	−15.1 ± 1.07	−5.93 ± 1.07	−0.98 ± 0.75	GC0256[n]; AAT118314[o]; T17-1665[y]	
201.410147	−43.084056	28 ± 9	r	−4.19 ± 0.36	−0.96 ± 0.35	0.59 ± 0.24	C156[l]; GC0258[n,r,u]; T17-1668[y]	3
201.434215	−42.983167	550 ± 34	q	−5.57 ± 1.71	1.58 ± 1.49	1.05 ± 1.05	HHH86-35[c,g,i,q]; GC0286[n,u]; T17-1724[y]	
201.443677	−42.581676	293 ± 115	o	−8.23 ± 0.76	−0.76 ± 1.05	−0.05 ± 0.44	GC0294[n]; AAT208206[o]; T17-1745[y]	
201.466443	−43.204605	187 ± 41	r	−9.60 ± 0.50	−0.72 ± 0.49	−0.18 ± 0.26	GC0592[r]; T17-1797[y]	
201.519553	−42.793058	336 ± 160	o	−0.49 ± 1.32	−5.68 ± 1.46	0.46 ± 0.66	GC0363[n]; AAT122794[o]; T17-1914[y]	
201.550553	−42.817643	225 ± 35	r	−2.88 ± 0.70	−5.63 ± 1.02	0.82 ± 0.38	GC0443[r]; T17-1964[y]	
201.566173	−42.916896	582 ± 10	s	−2.83 ± 0.74	−2.05 ± 0.88	−0.33 ± 0.42	f1.GC-22[i]; R122[m]; GC0382[n,r,s,x]; T17-1974[y]	
201.599416	−42.788083	343 ± 43	n	−10.9 ± 0.15	−4.85 ± 0.15	2.26 ± 0.07	HGHH-51[g]; GC0398[n]; T17-2015[y]	
201.599715	−43.295681	277 ± 158	o	−6.07 ± 1.47	−1.01 ± 2.46	−1.06 ± 0.84	GC0399[n]; AAT335187[o]; T17-2017[y]	
201.657114	−42.981575	276 ± 22	r	−5.66 ± 0.54	−13.0 ± 0.60	−0.17 ± 0.31	GC0553[r]; T17-2063[y]	
201.674875	−43.129149	271 ± 20	n	−50.3 ± 0.20	−11.7 ± 0.28	0.92 ± 0.11	HHH86-39[c,g,i,j,o]; GC0406[n,u]; T17-2078[y]	

Table 5
(Continued)

R.A. (deg J2000)	Decl. (deg J2000)	v_r (km s^{-1})	v_r References*	μ_α (mas yr^{-1})	μ_δ (mas yr^{-1})	ϖ (mas yr^{-1})	Names*	Notes
201.712004	−43.122378	372 ± 42	r	−10.1 ± 3.23	2.25 ± 4.16	2.13 ± 1.55	GC0557[r,u]; T17-2104[y]	
201.839971	−42.644833	252 ± 71	o	8.28 ± 0.49	−9.16 ± 0.59	0.29 ± 0.25	pff-gc-101[g,i,o]; GC0414[n]; T17-2180[y]	
201.753258	−42.360852	594 ± 102	o	−10.7 ± 1.26	−3.20 ± 1.30	0.17 ± 0.74	AAT223403[o]	

*See Table 1 for annotation references.

Notes: (1) This object was found to be a star based on HST/ACS imaging by Harris et al. (2006). (2) See Appendix C for information about the naming history of this object. (3) This object was identified as a GC based on HST/ACS imaging by Harris et al. (2006). It also has large ($\sigma \geqslant 4$) proper-motion and/or parallax measurements in Gaia DR2, and careful reinspection of its HST imaging confirms it to be a point source.

Table 6
Previously Classified Objects with Conflicting Measurements

R.A. (deg J2000)	Decl. (deg J2000)	v_r No. 1 (km s^{-1})	Source No. 1*	v_r No. 2 (km s^{-1})	Source No. 2*	Our Classification	Notes
200.689000	−43.011917	856 ± 56	m	16,000	n	Galaxy	1, 2
200.926424	−43.160459	357 ± 42	f		j	GC	3
200.986186	−43.000083	798 ± 49	m	13,000	n	Galaxy	1
201.011383	−42.809021	775 ± 75	m	5000	n	Galaxy	1
201.035905	−43.274189	305 ± 56	m		n	Star	4, 5
201.099937	−42.902944	582 ± 81	i	46,000	n	Unknown	6
201.117323	−42.884562	835 ± 83	m	13,000	n	Unknown	7
201.134014	−43.182469	636 ± 78	i		j	GC	8
201.137766	−43.312476	344 ± 58	f		k	Star	4, 9
201.144203	−43.214044	7717 ± 194	i	517 ± 123	m	Unknown	
201.188363	−43.388845	998 ± 250	m	17,000	n	Galaxy	1
201.203346	−43.271446	42,000	n	426 ± 41	r	Unknown	
201.232175	−43.379980	921 ± 146	m	9000	n	Galaxy	1
201.263696	−43.137316	31,000	n	690 ± 31	r	Unknown	
201.318460	−43.059162		k	352 ± 136	n	Star	4, 9
201.347769	−42.890588	2017 ± 78	i	545 ± 64	m	Unknown	
201.376149	−43.698210	317 ± 43	f	169 ± 108	n	Star	4
201.406112	−43.095806		l		This work	GC	10
201.415196	−43.067039	510 ± 33	f	32,124 ± 253	i	GC	11
201.440728	−42.571614	998 ± 250	m	15,000	n	Galaxy	1
201.455161	−43.000611	7349 ± 87	i	465 ± 30	q	Unknown	12
201.455309	−43.039000	384 ± 30	f	9942 ± 113	i	GC	13
201.543947	−43.018297	231 ± 143	n	311 ± 81	r	Unknown	
201.550553	−42.817643	117 ± 80	n	225 ± 35	r	Star	4, 14
201.572047	−43.110904	24,742 ± 79	i	513 ± 183	m	Unknown	
201.574090	−42.770562	64,000	n	178 ± 51	r	Galaxy	1
201.585963	−42.896082	271 ± 64	r		This work	Unknown	15
201.592072	−43.152950	505 ± 78	i	21,000	n	Unknown	16
201.660454	−42.762675	474 ± 65	f	2000	n	GC	17
201.705431	−43.082693	839 ± 63	m	15,000	n	Galaxy	1
201.748983	−42.924119	833 ± 32	m	13,000	n	Galaxy	1
202.076936	−42.553438	410 ± 42	f		This work	GC	18

*See Table 1 for annotation references.

Notes: (1) Based on visual inspection with PISCeS data, this object is a galaxy. (2) See discussion in Appendix B.2 about the position of this object in the literature. (3) This object also has a radial velocity measurement of 443 ± 48 km s^{-1} from Beasley et al. (2008), no parallax or proper motion, and a high-σ AEN value in Gaia DR2. We believe that the previous classification of this object as a foreground star is inaccurate (based on the shape of its PSF-subtracted residual by Gómez et al. 2006), so we include it in our confirmed GC sample. (4) Based on Gaia DR2 proper-motion and parallax data, we find this object to be a foreground star. It is also listed in Table 5. (5) This object was identified as a star by Beasley et al. (2008) because it exhibits strong molecular bands in its spectrum that are characteristic of an M-type star. (6) This object is also measured with $v_r = 606 \pm 33$ km s^{-1} in Woodley et al. (2010a), but they still listed the older velocity measurement of $v_r = 582 \pm 81$ as their "new weighted radial velocity." It was also noted as a background galaxy in Gómez et al. (2006) based on the shape of its PSF-subtracted residual. (7) Based on visual inspection with PISCeS data, at this position, there is a galaxy and an unknown point source–like object projected onto each other. (8) This object also has a radial velocity measurement of 775 ± 74 from Beasley et al. (2008) and 813 ± 40 from Woodley et al. (2010a), no parallax or proper motion, and a high-σ AEN value in Gaia DR2. We believe the classification as a background galaxy by Gómez et al. (2006) based on the shape of its PSF-subtracted residual is inaccurate, so we include it in our confirmed GC sample. (9) This object was found to be a star based on HST/ACS imaging by Harris et al. (2006). (10) This object was initially identified as a GC based on HST/ACS imaging by Harris et al. (2006), and it has two radial velocity measurements of 575 ± 36 (Woodley et al. 2007) and 524 ± 18 (Woodley et al. 2010b). In Gaia DR2, it has a proper-motion measurement with $\sigma = 4.12$, but in Gaia Early Data Release 3, it has a proper-motion measurement with only $\sigma = 1.5$. Because it is very close to the center of the galaxy, we believe the Gaia DR2 measurements to be inaccurate, so we include it in our confirmed GC sample. (11) This was also measured by Beasley et al. (2008) with $v_r = 557 \pm 49$ km s^{-1}. We believe the classification as a galaxy is inaccurate, so we include it in our confirmed GC sample. (12) This object is also measured with $v_r = 475 \pm 134$ in Woodley et al. (2010a), but they still listed the older velocity measurement of $v_r = 465 \pm 30$ as their "new weighted radial velocity." (13) This object was also measured by Beasley et al. (2008) to have $v_r = 420 \pm 51$ and by Woodley et al. (2010a) to have $v_r = 371 \pm 28$. We believe the classification as a galaxy is inaccurate, so we include it in our confirmed GC sample. (14) Woodley et al. (2010a) classified a small number of candidates as GCs with low velocities based on their structural parameters, many of which we find to actually be foreground stars. (15) This object has one radial velocity measurement of 271 ± 64 km s^{-1} but also has stellar AEN and C_{3-6} values. It has no reported proper motion or parallax in Gaia DR2. We recommend that further study of this GC more confidently reinforce or oppose its status as a GC of NGC 5128. (16) This object is also measured with $v_r = 357 \pm 35$ km s^{-1} in Woodley et al. (2010a), but they still listed the older velocity measurement of $v_r = 505 \pm 78$ as their "new weighted radial velocity." (17) The position of this target is listed by Peng et al. (2004) and Beasley et al. (2008) as 201.65829, −42.763861, which is 7″ away from the position we and other follow-up studies find for this GC. It also has additional radial velocity measurements of 492 ± 37 km s^{-1} in Woodley et al. (2007) and 627 ± 21 km s^{-1} in Woodley et al. (2010a). (18) This object has a Gaia DR2 proper-motion measurement of 13.47 ± 2.68 mas yr^{-1}. We do not include it in Table 5, however, because it has AEN, parallax, color, and C_{3-6} values and two independent radial velocity measurements consistent with its status as a GC in NGC 5128. Therefore, it is recorded in Table 4 but not included in the fiducial sample, Figure 12, or Table 5.

sources, if applicable. We also include our classification of each object, as well as further information indicated by the "Notes" column.

Many sources experience a discrepancy between Woodley et al. (2007) and Beasley et al. (2008). It appears that between sharing data with the Woodley group and publishing their own paper, the Beasley group updated measurements on several targets. We note that one of these objects has a mismatch in both its velocity measurement and coordinates. Woodley et al. (2007) gave an incorrect position for HH-048 as $\alpha = 200.^{\circ}68900$, $\delta = -43.^{\circ}119111$, with a radial velocity of $856 \pm 56\,\mathrm{km\,s^{-1}}$, citing Beasley et al. (2008) as the reference for this radial velocity measurement. Beasley et al. (2008), however, listed HH-048 as a background galaxy ($v_r = 16{,}000\,\mathrm{km\,s^{-1}}$) with the same R.A. but a decl. of $\delta = -43.^{\circ}011917$ (note the single difference in the digit following the decimal point). Based upon visual inspection, the position listed in the Beasley catalog is correct and listed in Table 6.

Appendix C
An Object with Too Many Names

During our literature review, we found an instance where two confirmed GCs with different names shared the same position. The objects identified most recently as GC 0462/T17-1560 and GC 0200/T17-1561 have the same position in the Sinnott et al. (2010) catalog and positions that differ by 0.″24 in the T17 catalog. Upon visual inspection, both objects seem to correspond to the GC originally identified as HGHH-46 in the Harris et al. (1992) catalog. The discrepancy appears to have begun when the GC was reported in the "New Radial Velocity Measurements of Known Globular Clusters" table in Woodley et al. (2010b), even though it had already been identified by previous surveys. Based on the object's high proper motion in Gaia DR2, we have determined that it is actually a foreground star rather than a GC in NGC 5128; see Appendix B.1 for details. We list all of the names for this object in Table 5 in the hope of avoiding future confusion.

Appendix D
Background Galaxy Positions that Point to Empty Sky

When compiling our list of radial velocity–confirmed background galaxies, we found three instances of positions pointing to empty sky in the PISCeS data set rather than an object, based upon visual inspection. These were originally noted in Harris et al. (2004) as new GC candidates and confirmed as background galaxies by Woodley et al. (2005) based on radial velocity measurements. Both of these papers generally have consistent astrometry with PISCeS data, except for these instances. The three positions in question are: (1) $\alpha = 201.^{\circ}01875$, $\delta = -42.^{\circ}804500$, ID: 283; (2) $\alpha = 201.^{\circ}02288$, $\delta = -42.^{\circ}790028$, ID: 285; and (3) $\alpha = 201.^{\circ}25537$, $\delta = -42.^{\circ}907361$, ID: 299, where all positions are in J2000 coordinates. We do not include these objects when calculating the fidelity of our extended galaxy checks in Section 4.3.

ORCID iDs

Allison K. Hughes https://orcid.org/0000-0002-1718-0402
David J. Sand https://orcid.org/0000-0003-4102-380X
Anil Seth https://orcid.org/0000-0003-0248-5470
Jay Strader https://orcid.org/0000-0002-1468-9668
Karina Voggel https://orcid.org/0000-0001-6215-0950
Antoine Dumont https://orcid.org/0000-0003-0234-3376
Denija Crnojević https://orcid.org/0000-0002-1763-4128
Nelson Caldwell https://orcid.org/0000-0003-2352-3202
Joshua D. Simon https://orcid.org/0000-0002-4733-4994
Puragra Guhathakurta https://orcid.org/0000-0001-8867-4234
Elisa Toloba https://orcid.org/0000-0001-6443-5570

References

Ahumada, R., Allende Prieto, C., Almeida, A., et al. 2020, ApJS, 249, 3
Alabi, A. B., Forbes, D. A., Romanowsky, A. J., et al. 2016, MNRAS, 460, 3838
Beasley, M. A. 2020, in Reviews in Frontiers of Modern Astrophysics: From Space Debris to Cosmology, ed. P Kabáth et al. (Berlin: Springer)
Beasley, M. A., Bridges, T., Peng, E., et al. 2008, MNRAS, 386, 1443
Beasley, M. A., & Trujillo, I. 2016, ApJ, 830, 23
Bertin, E. 2010, SWarp: Resampling and Co-adding FITS Images Together, Astrophysics Source Code Library, ascl:1010.068
Bertin, E., & Arnouts, S. 1996, A&AS, 117, 393
Bica, E., Bonatto, C., Barbuy, B., & Ortolani, S. 2006, A&A, 450, 105
Boubert, D., & Everall, A. 2020, MNRAS, 497, 4246
Brodie, J. P., Romanowsky, A. J., Strader, J., et al. 2014, ApJ, 796, 52
Brodie, J. P., & Strader, J. 2006, ARA&A, 44, 193
Crnojević, D., Sand, D. J., Bennet, P., et al. 2019, ApJ, 872, 80
Crnojević, D., Sand, D. J., Caldwell, N., et al. 2014, ApJL, 795, L35
Crnojević, D., Sand, D. J., Spekkens, K., et al. 2016, ApJ, 823, 19
Cutri, R. M., Skrutskie, M. F., van Dyk, S., et al. 2003, VizieR On-line Data Catalog: II/246, 2MASS All Sky Catalog of Point Sources
de Vaucouleurs, G., de Vaucouleurs, A., Corwin, H. G., Jr., et al. 1991, S&T, 82, 621
Dufour, R. J., van den Bergh, S., Harvel, C. A., et al. 1979, AJ, 84, 284
Durrell, P. R., Côté, P., Peng, E. W., et al. 2014, ApJ, 794, 103
El-Badry, K., Quataert, E., Weisz, D. R., Choksi, N., & Boylan-Kolchin, M. 2019, MNRAS, 482, 4528
Evans, D. W., Riello, M., De Angeli, F., et al. 2018, A&A, 616, A4
Fahrion, K., Müller, O., Rejkuba, M., et al. 2020, A&A, 634, A53
Faifer, F. R., Forte, J. C., Norris, M. A., et al. 2011, MNRAS, 416, 155
Forbes, D. A. 2017, MNRAS, 472, L104
Forbes, D. A., Ponman, T., & O'Sullivan, E. 2012, MNRAS, 425, 66
Forbes, D. A., & Remus, R.-S. 2018, MNRAS, 479, 4760
Gaia Collaboration, Brown, A. G. A., Vallenari, A., et al. 2018a, A&A, 616, A1
Gaia Collaboration, Brown, A. G. A., Vallenari, A., et al. 2018b, A&A, 616, A1
Gaia Collaboration, Brown, A. G. A., Vallenari, A., et al. 2021, A&A, 649, A1
Georgiev, I. Y., Hilker, M., Puzia, T. H., Goudfrooij, P., & Baumgardt, H. 2009, MNRAS, 396, 1075
Georgiev, I. Y., Puzia, T. H., Goudfrooij, P., & Hilker, M. 2010, MNRAS, 406, 1967
Gómez, M., Geisler, D., Harris, W. E., et al. 2006, A&A, 447, 877
Graham, J. A. 1979, ApJ, 232, 60
Graham, J. A., & Phillips, M. M. 1980, ApJL, 239, L97
Harris, G. L. H. 2010, PASA, 27, 475
Harris, G. L. H., Geisler, D., Harris, H. C., & Hesser, J. E. 1992, AJ, 104, 613
Harris, G. L. H., Gómez, M., Harris, W. E., et al. 2012, AJ, 143, 84
Harris, G. L. H., Harris, W. E., & Geisler, D. 2004, AJ, 128, 723
Harris, G. L. H., Rejkuba, M., & Harris, W. E. 2010, PASA, 27, 457
Harris, W. E. 1991, ARA&A, 29, 543
Harris, W. E. 2001, in Saas-Fee Advanced Course 28: Star Clusters, ed. L. Labhardt & B. Binggeli (Berlin: Springer), 223
Harris, W. E., Harris, G. L. H., Barmby, P., McLaughlin, D. E., & Forbes, D. A. 2006, AJ, 132, 2187
Harris, W. E., Harris, G. L. H., Holland, S. T., & McLaughlin, D. E. 2002, AJ, 124, 1435
Harris, W. E., & van den Bergh, S. 1981, AJ, 86, 1627
Hesser, J. E., Harris, H. C., & Harris, G. L. H. 1986, ApJL, 303, L51
Holland, S., Côté, P., & Hesser, J. E. 1999, A&A, 348, 418
Hui, X., Ford, H. C., Freeman, K. C., & Dopita, M. A. 1995, ApJ, 449, 592
Jennings, Z. G., Strader, J., Romanowsky, A. J., et al. 2014, AJ, 148, 32
Jester, S., Schneider, D. P., Richards, G. T., et al. 2005, AJ, 130, 873
Jordán, A., McLaughlin, D. E., Côté, P., et al. 2007, ApJS, 171, 101
Ko, Y., Lee, M. G., Park, H. S., et al. 2019, ApJ, 872, 202

Landsman, W. B. 1993, in ASP Conf. Ser. 52, Astronomical Data Analysis Software and Systems II, ed. R. J. Hanisch, R. J. V. Brissenden, & J. Barnes (San Francisco, CA: ASP), 246
Lee, M. G., & Jang, I. S. 2016, ApJ, 822, 70
Mackey, A. D., Ferguson, A. M. N., Huxor, A. P., et al. 2019, MNRAS, 484, 1756
Mackey, A. D., Huxor, A. P., Ferguson, A. M. N., et al. 2010, ApJL, 717, L11
Marigo, P., Girardi, L., Bressan, A., et al. 2008, A&A, 482, 883
Martini, P., & Ho, L. C. 2004, ApJ, 610, 233
McConnachie, A. W., Irwin, M. J., Ibata, R. A., et al. 2009, Natur, 461, 66
McLaughlin, D. E., Barmby, P., Harris, W. E., Forbes, D. A., & Harris, G. L. H. 2008, MNRAS, 384, 563
McLeod, B., Geary, J., Conroy, M., et al. 2015, PASP, 127, 366
Mouhcine, M., Harris, W. E., Ibata, R., & Rejkuba, M. 2010, MNRAS, 404, 1157
Müller, O., Fahrion, K., Rejkuba, M., et al. 2021, A&A, 645, A92
Muñoz, R. P., Puzia, T. H., Lançon, A., et al. 2014, ApJS, 210, 4
Nidever, D. L., Dey, A., Fasbender, K., et al. 2021, AJ, 161, 192
Nidever, D. L., Dey, A., Olsen, K., et al. 2018, AJ, 156, 131
Park, H. S., & Lee, M. G. 2013, ApJL, 773, L27
Peng, E. W., Ferguson, H. C., Goudfrooij, P., et al. 2011, ApJ, 730, 23
Peng, E. W., Ford, H. C., & Freeman, K. C. 2004, ApJS, 150, 367
Peng, E. W., & Lim, S. 2016, ApJL, 822, L31
Pota, V., Brodie, J. P., Bridges, T., et al. 2015, MNRAS, 450, 1962
Powalka, M., Lançon, A., Puzia, T. H., et al. 2016a, ApJS, 227, 12
Powalka, M., Puzia, T. H., Lançon, A., et al. 2016b, ApJL, 829, L5
Rejkuba, M., Dubath, P., Minniti, D., & Meylan, G. 2007, A&A, 469, 147
Rhode, K. L., & Zepf, S. E. 2001, AJ, 121, 210
Sand, D. J., Crnojević, D., Strader, J., et al. 2014, ApJL, 793, L7
Schlafly, E. F., & Finkbeiner, D. P. 2011, ApJ, 737, 103
Schlegel, D. J., Finkbeiner, D. P., & Davis, M. 1998, ApJ, 500, 525
Silge, J. D., Gebhardt, K., Bergmann, M., & Richstone, D. 2005, AJ, 130, 406
Sinnott, B., Hou, A., Anderson, R., Harris, W. E., & Woodley, K. A. 2010, AJ, 140, 2101
Strader, J., Caldwell, N., & Seth, A. C. 2011, AJ, 142, 8
Taylor, M. A., Muñoz, R. P., Puzia, T. H., et al. 2016, arXiv:1608.07285
Taylor, M. A., Puzia, T. H., Gomez, M., & Woodley, K. A. 2015, ApJ, 805, 65
Taylor, M. A., Puzia, T. H., Harris, G. L., et al. 2010, ApJ, 712, 1191
Taylor, M. A., Puzia, T. H., Muñoz, R. P., et al. 2017, MNRAS, 469, 3444
Toloba, E., Sand, D. J., Spekkens, K., et al. 2016, ApJL, 816, L5
van den Bergh, S., Hesser, J. E., & Harris, G. L. H. 1981, AJ, 86, 24
Veljanoski, J., Mackey, A. D., Ferguson, A. M. N., et al. 2014, MNRAS, 442, 2929
Voggel, K. T., Seth, A. C., Neumayer, N., et al. 2018, ApJ, 858, 20
Voggel, K. T., Seth, A. C., Sand, D. J., et al. 2020, ApJ, 899, 140
Wasserman, A., Romanowsky, A. J., Brodie, J., et al. 2018, ApJ, 863, 130
Whitmore, B. C., Zhang, Q., Leitherer, C., et al. 1999, AJ, 118, 1551
Wilkinson, A., Sharples, R. M., Fosbury, R. A. E., & Wallace, P. T. 1986, MNRAS, 218, 297
Woodley, K. A., Gómez, M., Harris, W. E., Geisler, D., & Harris, G. L. H. 2010a, AJ, 139, 1871
Woodley, K. A., Harris, W. E., Beasley, M. A., et al. 2007, AJ, 134, 494
Woodley, K. A., Harris, W. E., & Harris, G. L. H. 2005, AJ, 129, 2654
Woodley, K. A., Harris, W. E., Puzia, T. H., et al. 2010b, ApJ, 708, 1335